

## C-1. Statistical verification of short range forecasts by NHM and WRF-ARW with coarse resolution<sup>1</sup>

### C-1-1. Introduction

In Southeast Asian countries, meteorological disasters (e.g. heavy rainfall, floods, windstorms) frequently occur, causing severe damages. To reduce such meteorological disasters, NHM is used as a community model in the NWP system for predicting the occurrence of severe meteorological phenomena. To apply NHM to NWP in Southeast Asia, the verification of its forecast accuracy in the tropics is important. We selected 20 km as the horizontal resolution to reduce the lateral boundary nesting gap for the global data (about 100km resolution). In addition, verifications with WRF-ARW (Skamarock et al. 2005; hereafter WRF) were conducted using the same conditions and domains in order to check the performance of NHM relative to WRF.

In this section, the coarse resolution (20 km) results are documented. The fine resolution (5 km) results with 1-way nesting from 20 km results are described in the next section (C-2).

### C-1-2. Model description and design of experiments

The same domain size, the same horizontal resolution, the same model top height and the same time step are used to ensure a fair comparison. Initial and boundary conditions are taken from the global forecast system of the National Centers for Environmental Prediction (NCEP-GFS) every 3 hours.

The model specifications and parameters settings in the experiments use the recommended (default) values without tuning (Tab. C-1-1). The same settings in each model are applied to two regions, Japan and Southeast Asia.

Two simulation periods are selected. One is 15 days from 1 to 15 July 2007, which is the rainy season in Japan and the dry season in Java Island, Indonesia. Another period is 15 days from 1 to 15 January 2008, which is the winter heavy snow season in Japan and the rainy season in Java Island. Simulations for 1.5-day (36 hours) forecasts are conducted from 00 UTC for 15 days and latter 24 hours results are verified.

### C-1-3. Statistical verification results

Figures C-1-1a~c indicate the continuous 15 day accumulated precipitation around Japan in July 2007. The observed precipitation area by passive microwave satellites (Fig. C-1-1a), corresponding to

**Table C-1-1. Model descriptions.**  
After Hayashi et al. (2008)

	NHM ver.2008-Aug-20	WRF-ARW ver.2.2.1	
Domain size and forecast hour	150 x 150 grid in horizontal and 40 layer in vertical 20km in horizontal resolution model top height = 22km (about 45 hPa) (vertical coordinate: NHM = z-star, WRF = $\eta$ ) forecast hour = 36hour (dt = 75sec, 1728 steps)		
Initial / Boundary conditions	NCEP-GFS forecast 00UTC, 0-36 hr. (every 3 hr.), 1 x 1 degree horizontal resolution		
Experimental settings	cloud microphysics	6-class bulk microphysics	3-class with simple ice
	cumulus parameterization	Kain-Fritsch scheme (not exactly the same)	
	radiation	GSM0412 scheme	RRTM for longwave Dudhia for shortwave
	boundary layer	Improved Mellor-Yamada Lv. 3	YSU scheme
	land surface	Thermal diffusion scheme (4-layer)	Thermal diffusion scheme (5-layer)
	lateral(L) and upper(U) boundary	L: Rayleigh damping (200km) U: Rayleigh damping (7km)	L: specified boundary(100km) U: no damping
	full formulations	Saito et al. (2007)	Skamarock et al. (2005)
	parameter file for whole settings in the experiments	Nhm/Ss/RF20km/fcst.sh Using these recommended namelists without tuning	WRFV2/test/em_real/namelist.input

<sup>1</sup> S. Hayashi

the Baiu-front in south Japan, is well reproduced by the models (Figs. C-1-1b and c). In contrast, the precipitation over the western part of Japan and the Sea of Japan are overestimated in the models.

Figures C-1-1d~f are the same as Figs. C-1-1a~c except for January 2008. In this period, the heavy snowfall was retrieved over northwestern coast of the main Island of Japan. CMORPH (Fig. C-1-1d), however, does not yield an exact snowfall precipitation amount for Japan's main island, because snow and ice on a surface cannot be distinguished from frozen hydrometeors by the present precipitation estimation algorithm of CMORPH. Compared with surface observation (AMeDAS), the heavy snow fall was found to be well reproduced (figure not shown).

Figures C-1-1g~i are the same as Figs. C-1-1a~c, but for July 2007 over the maritime continent. This period correspond to the dry season in the Java Island. Both models reproduce the dry climate on Java Island well (Figs. C-1-1h and i). However, the predicted precipitation is overestimated in the northern part of the domain, especially near the north boundary of the WRF result (the edge regions of 300 km width are excluded from the statistical verification).

Figures C-1-1j~l are the same as Figs. C-1-1d~f except for Southeast Asia. The accumulated precipitation over the sea is overestimated in both models (Figs. C-1-1k and l). In addition, WRF results in excessive precipitation over the Borneo Island.

Figures C-1-2a~d show the threat scores for 3-hour precipitation against CMORPH or AMeDAS. A 40 km verification grid size were used in order to avoid the differences between the map projections of CMORPH and the models. The threat scores for both models in July over Japan are 0.27 at 1 mm / 3 hours for CMORPH (Fig. C-1-2a). This value is not far from that of JMA's operational mesoscale model (MSM; the horizontal resolution is 5km). Figure C-1-2b shows the threat score for the wintertime in Japan. The threat scores for two models against CMORPH are less than half of those for July 2007 over Japan. Meanwhile, the deteriorations in the threat scores for the models against AMeDAS were smaller than those against CMORPH. Therefore, the decreasing scores against CMORPH are not caused by the models but by snow on a land surface. The threat scores for both models over Southeast Asia are 0.12-0.14 at 1 mm / 3-hours (Figs. C-1-2c,d), which are about half of the scores in July 2007 over Japan.

In our results, the accuracy of both forecast models around Southeast Asia was worse than that of the forecast for the rainy season in Japan. One of the reasons is that precipitation in the rainy season in Japan is caused by a mid-latitude synoptic disturbance, while tropical precipitation is mainly caused by convection. Other causes may be in the initial and boundary conditions and / or the physical processes of the two models. The accuracy of current global models of coarser grid resolutions may be insufficient for forecasting precipitation in the tropics. In addition, both of the mesoscale models may have some problems or unsuitable settings for forecasting tropical precipitation. We need to obtain more accurate statistical verification of the models.

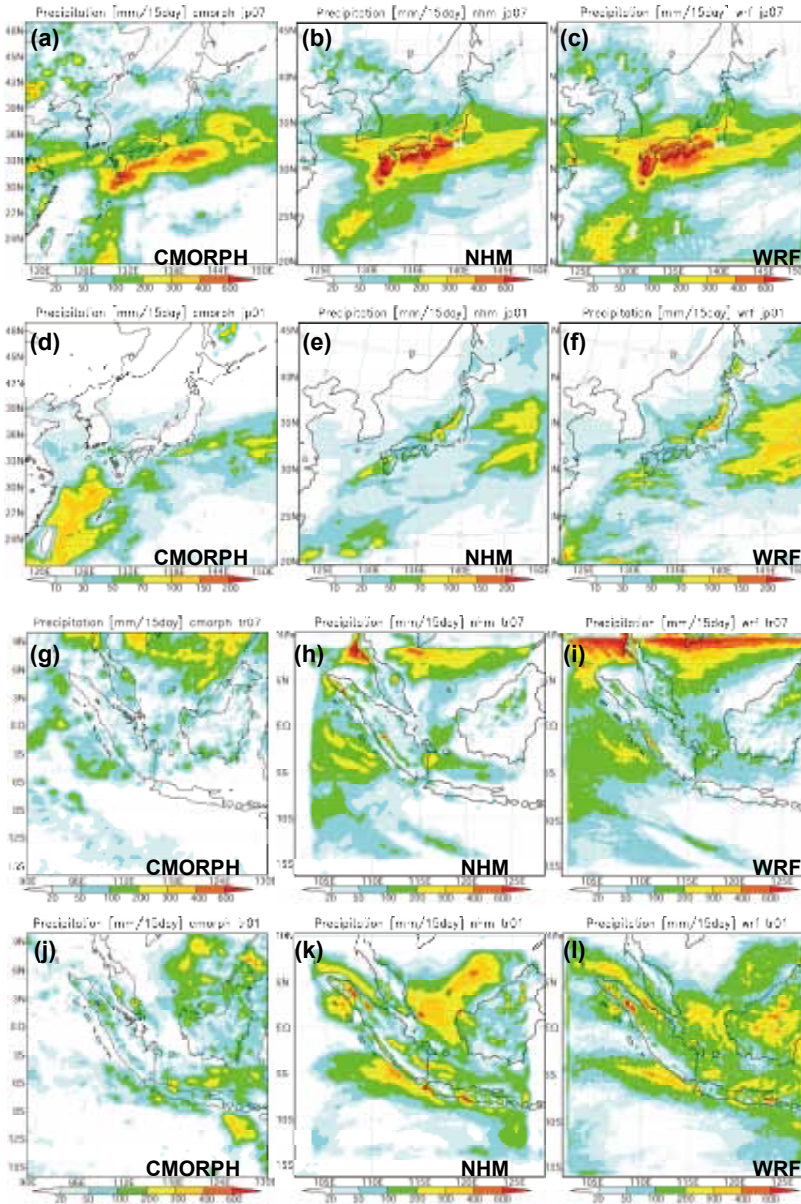


**Fig. C-1-1.**  
(a, b, c): 15 days accumulated precipitation from 1 to 15 July 2007 around Japan. (a) CMORPH, (b) NHM, (c) WRF,

(d, e, f): Same as (a, b, c) except from 1 to 15 January 2008,

(g, h, i): Same as (a, b, c) except around Southeast Asia,

(j, k, l): Same as (g, h, i) except from 1 to 15 January 2008,

After Hayashi et al. (2008).

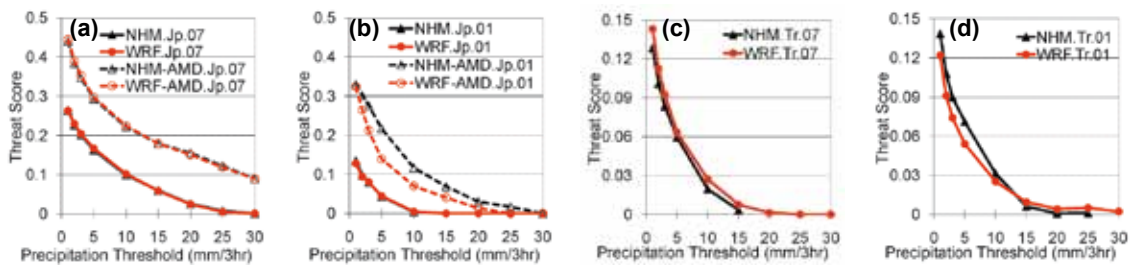


**Fig. C-1-2.** 3-hour precipitation threat scores, (a) from 1 to 15 July 2007 (b) from 1 to 15 January 2008 around Japan, and (c, d) same as (a, b) except around Southeast Asia. Solid lines show scores against CMORPH and dashed lines show scores against AMEDAS in (a) and (b). After Hayashi et al. (2008).

## C-2. Statistical verification of short-range forecasts by the NHM and WRF-ARW models with fine resolution<sup>1</sup>

### C-2-1. Introduction

As described in Section C-1, the NWP accuracy over Southeast Asia by models of 20-km horizontal resolution (JMA's nonhydrostatic model NHM and Weather Research Forecasting model WRF-ARW) was worse than that over Japan. We conducted fine-resolution experiments to investigate how forecast accuracy improves by using 5-km horizontal resolution.

### C-2-2. Model description and design of experiments

Almost the same settings as listed in Table C-1-1 were used (Table C-2-1). The domain size of the 20-km models was slightly expanded from that in section C-1 to avoid the influence of the lateral boundaries on the 5-km model. We updated both models to their latest versions (NHM ver. 3.1 and WRF-ARW ver. 3.1.1) and updated their default settings (details are described in Section C-2-5). It is notable that NHM's default parameter settings employ a six-class bulk cloud microphysics scheme that predicts number concentrations of cloud ice.

For the Southeast Asia region, 30-hour forecasts from 0600 UTC on each of 31 days in January 2008 were conducted with a 5-km horizontal resolution nested into the 20-km model forecasts with initial times of 0000 UTC. For the Japan region, similar 24-hour forecasts were conducted for July 2007 and analyzed at both resolutions.

### C-2-3. Statistical verification results

Figures C-2-1 presents the horizontal distribution of the 31 days of accumulated precipitation in July 2007 in the Japan region from CMORPH satellite precipitation observations and models. Compared with the satellite observations (Fig. C-2-2a), the forecasts from the 20-km horizontal resolution models (Figs. C-2-2b and c) well reproduced the location and precipitation of the Baiu-front. So did the 5-km models (Figs. C-2-2e and f), however, the precipitation amounts were overestimated on the south side of the Japanese Islands compared with CMORPH observations.

Both 5-km models represented detailed precipitation distributions. Figure C-2-1d shows the 1-km grid radar precipitation amounts calibrated by surface rain gauges (called Radar-AMeDAS, hereafter

Table C-2-1. Model descriptions.

	NHM v3.1 (release candidate)	WRF-ARW v3.1.1
Domain size and forecast period	160x160 grids for 20km resolution in horizontal 301x301 grids for 5km resolution in horizontal 40 layers in vertical, model top 22km (about 45 hPa) (vertical coordinate: NHM = z-star, WRF = η) forecast hour = 36 hour for 20km, 30 hour for 5km in every 31 days	
Initial / Boundary	NCEP-GFS forecast at 00UTC for initial and every 3hr forecast for boundary 1x1 degree horizontal resolution, 24 P-levels	
model configurations	Nhm/Ss/Rf20km/est.sh (for 20km) Rfnest/est.sh (for 5km)	WRFV3/test/eri_real/ namelist.input
	Using these configurations <b>without tuning</b>	
cloud microphysics	6-class bulk with number of ice	3-class bulk with simple ice
cumulus parameterization	Modified Kain-Fritsch scheme	Kain-Fritsch scheme
radiation	GSM0412 scheme	RRM for longwave, Dudhia for shortwave
boundary layer	Improved MYNN3	YSU scheme
Lateral and Upper boundary	damping for lateral and upper boundary	no damping for upper boundary, only for lateral
others	almost the same configurations as JMA operational 5km model OMS0	

<sup>1</sup> S. Hayashi

R-A). The R-A precipitation data have better resolution and more accurate amounts for the Japanese Islands than the CMORPH data. The topographic influence on precipitations was clearly indicated in the R-A data, especially on the south side of Kyushu and Shikoku islands, and the Kii Peninsula. Both the 5-km models well reproduced these details (Fig. C-2-2e and f). Over the San-in area, however, both models overestimated the precipitation. The horizontal spread of the precipitation distribution from WRF was larger than that of observations, and the results of NHM.

Figures C-2-2 depicts the horizontal distribution of the accumulated precipitation for January 2008 over Southeast Asia from observations and models. Compared with the satellite observation (Fig. C-2-2a), all the models overestimated precipitation amounts over the almost all domains (Figs. C-2-2b~e). In particular, WRF-20km over-predicted precipitation over Borneo and Sumatra. Both 5-km models produced the details of the precipitation distribution, especially the orographic precipitation in Sumatra by NHM-5km. It is difficult to verify the detailed precipitation distributions because the resolution of CMORPH data is insufficient to model this fine structure.

To compare CMORPH data against the precipitation models, the equitable threat scores (ETSs) for the 3-hour precipitation in each 40-km verification grid, in order to avoid the differences from the map projections and horizontal resolution between CMORPH and the models, are shown in Figures C-2-3a for Japan C-2-3c for Southeast Asia, and Figure C-2-3b shows the ETS of 3-hour precipitation against AMeDAS rain gauges for Japan. The ETSs against CMORPH for Japan were the same for both the 5-km and the 20-km models (Fig. C-2-3a). The ETSs of the 5-km models against AMeDAS, however, were better than those of the 20-km models (Fig. C-2-3b). In particular, the ETSs of NHM-5km were clearly superior for moderate and strong (10 mm and 40 mm) 3-hour precipitations to those of NHM-20km. The ETSs of the 5-km models for Southeast Asia were slightly better than those of the 20-km models. However, their values were much lower than those for Japan (Fig. C-2-3a).

In addition, we conducted some sensitivity experiments for both Japan and Southeast Asia. First, NHM-5km and WRF-5km without cumulus parameterization reproduced almost the same precipitation distribution as the models with cumulus parameterization (figures not shown). Second, WRF-5km with the parameter settings by the Developmental Testbed Center (<http://www.dtcenter.org/>) also yielded similar results (figures are not shown). Third, both models were run with a 1.25-km horizontal resolution, but they did not improve upon the 5-km models (figures are not shown). We intend to future subject to investigate ways to improve forecasts in the tropics.

#### **C-2-4. Summary**

We found that models with 5-km resolution produced better forecast than models with 20-km resolution. The difference was greater for Japan than for Southeast Asia region, and the scores for Southeast Asia were worse than those for Japan. The accuracy of NHM was better than that of WRF in these experiments. Better verifications methods using finer scale observations are needed to investigate ways to improve forecasts in tropics.

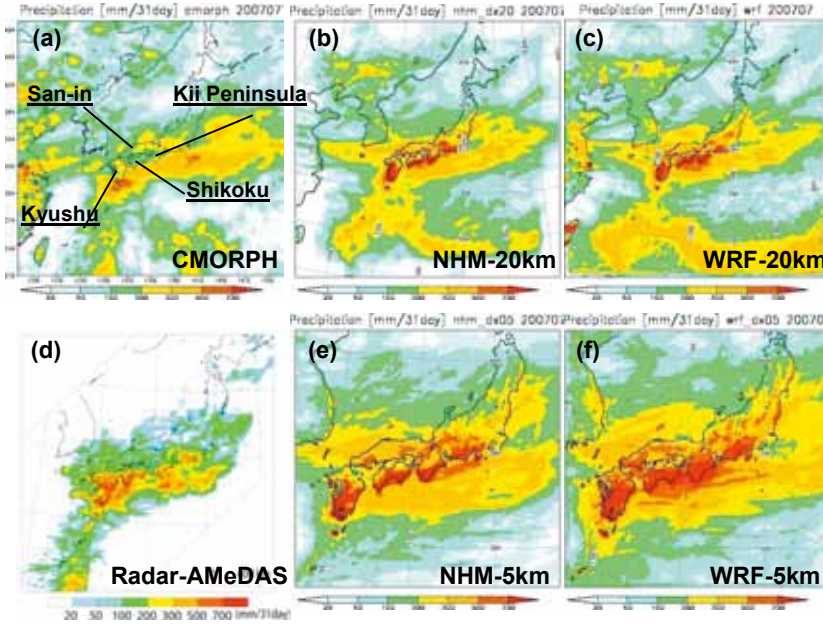


**Fig. C-2-1.**  
 (a, b, c, d, e, f): 31 days Accumulated Precipitation from 1 to 31 July 2007 around Japan.  
 (a) CMORPH, (b) NHM-20km, (c) WRF-20km, (d) Radar-AMeDAS, (e) NHM-5km, (f) WRF-5km

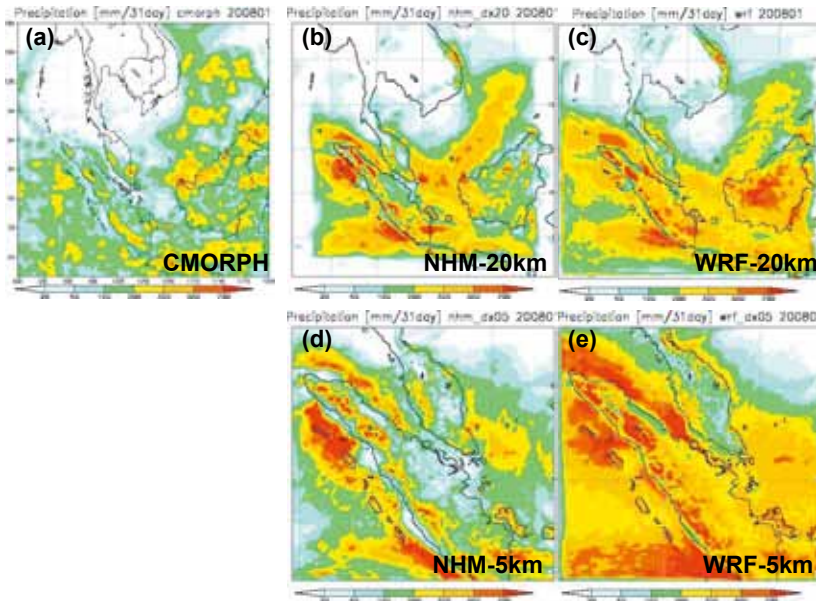


**Fig. C-2-2.**  
 (a, b, c, d, e): 31 days Accumulated Precipitation from 1 to 31 January 2008 around Southeast Asia.  
 (a) CMORPH, (b) NHM-20km, (c) WRF-20km, (d) NHM-5km, (e) WRF-5km

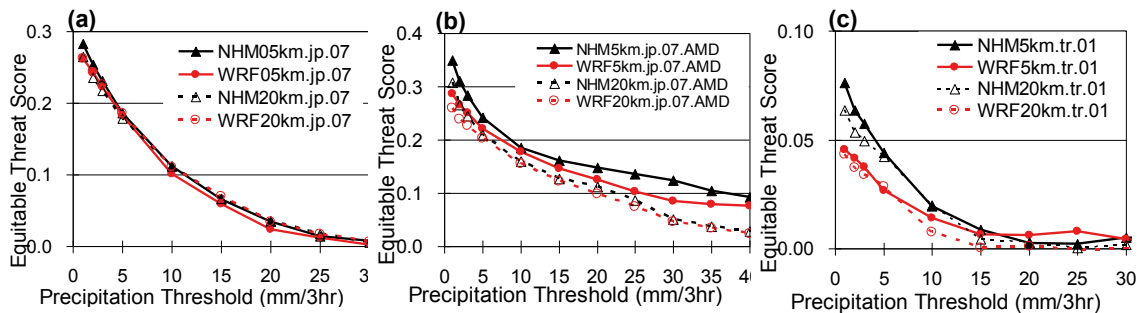


**Fig. C-2-3.** 3-hour precipitation equitable threat scores, (a) against CMORPH for July 2007 in Japan, (b) against AMeDAS for July 2007 in Japan, (c) against CMORPH for January 2008 in Southeast Asia. Black lines represent NHM, red lines represent WRF, solid lines are for 5-km models and dashed lines for 20-km models.

### C-2-5. Supplement on updates in both the models

In this research, NHM was updated from ver. 2.00-MSM0808 (Section C-1) to ver. 3.1 (release-candidate), and WRF-ARW was updated from ver. 2.2.1 (Section C-1) to ver. 3.1.1. Updated points are listed below.

#### a. NHM updates from ver. 2.00-MSM0808 to ver. 3.1

- Cloud microphysics scheme was changed from a six-class one-moment scheme to six-class one-moment with cloud-ice two-moment scheme.
- Radiation scheme was updated to implement aerosol monthly climatological value, effective radius of cloud ice, and emissivity correction for cloud fraction.
- Nonlinear diffusion coefficient was changed. The test of double nested NHM-5km in the tropics, produced undesirable overestimation of the amount of upper-level clouds (hereafter CH). Simulated CH from NHM-5km was almost 100 % cloud-amount over the whole model domain (Fig. C-2-4a). This overestimation led to underestimation of diurnal change of surface soil/air temperatures through the shortage of short-wave solar radiation.

Sensitivity tests revealed that the overestimation of CH was caused by inappropriate application of the nonlinear computational diffusion to the number concentration of cloud ice (hereafter QNCI) (Fig. C-2-4b). In NHM, a third-order nonlinear damping and a fourth-order linear damping (Eqs. G4-1 and G4-2 in Saito et al. 2001) were employed as the computational diffusion. The magnitude of the third-order nonlinear damping was set in the NAMELIST parameter 'DIFNL'. For two-grid noises of amplitude  $-a$ , the nonlinear damping gives the equivalent  $1/e$ -folding time  $DIFNL * \Delta t / a$  when  $DIFNL > 0$ , and  $|DIFNL| / a$  when  $DIFNL < 0$ . Because QNCI sometimes takes a very large value (on the order of  $10^6$ ), QNCI is diffused excessively by application of the nonlinear computational diffusion, yielding overextension of CH. In the experiment in Section C-2-3, we changed DIFNL from -600 to -2400 to weaken this nonlinear diffusion.

After NHM ver. 3.2, the nonlinear diffusion is no longer applied to cloud microphysical quantities except for the mixing ratios of water vapor, cloud water, and cloud ice.

- Some trivial bugs were fixed.

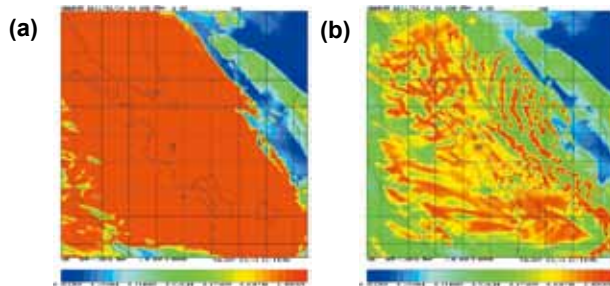


**Fig. C-2-4.** (a) Simulated upper-level cloud amount (CH) at FT=6-hour when nonlinear diffusion is applied to QNCI. (b) Simulated CH at FT=6-hour nonlinear diffusion is not applied to QNCI.

#### b. WRF-ARW update from ver. 2.2.1 to ver. 3.1.1

- Land surface scheme was changed from thermal diffusion scheme to Noah-LSM
- Upper-level damping coefficient was changed from 0.01 to 0.2.
- A positive definite advection scheme for moist and scalar variables was applied.
- Some trivial bugs were fixed.

### C-3. Structure of the regional heavy rainfall system that occurred in Mumbai, India on 26 July 2005<sup>1</sup>

Heavy rainfalls frequently occur not only in Japan, but also in other countries, especially in southeastern or southern Asian countries. According to the Asian Disaster Reduction Center (ADRC)-Natural Disasters Data Book-2006 (ADRC 2007), the most frequent disasters in member countries (India, Indonesia, Viet Nam, and 22 other countries) are windstorms and floods. These phenomena account for 80% of the disasters affecting the population in the Asian and ADRC member countries.

In this study, the heavy rainfall that occurred at Santa Cruz, a suburb of Mumbai, on 26 July 2005 was investigated. Due to this heavy rainfall, the 24 hour rainfall amount at Santa Cruz reached 944.2 mm (Bohra et al. 2005). The rainfall amount recorded in this event was about a half of the annual rainfall. Because the heavy rainfall was caused by a regional convective system, we reproduced the heavy rainfall by the downscale experiments using a non-hydrostatic model with a fine horizontal grid interval (JMA-NHM; Saito et al. 2006). Probability and formation factors of the heavy rainfall were also investigated by ensemble forecasts.

#### C-3-1. Observed features of the heavy rainfall

According to Bohra et al. (2005), the rainfall at Santa Cruz started at 0600 UTC (11.5 India Standard Time (IST)) on 26 July 2005, and continued for 18 hours (Fig. C-3-1a). The rainfall region observed by the Tropical Rainfall Measuring Mission (TRMM) satellite revealed that the horizontal scale of this rainfall event was several tens of kilometers (Fig. C-3-1b). These observed results indicated that the rainfall system had a long-lasting structure that brought a large quantity of rainfall to a small region. Figure C-3-1c illustrates the precipitable water vapor (PWV) observed by the Special Sensor Microwave/ Imager (SSM/I). When the heavy rainfall occurred, a region of large PWV over 60 mm existed just north of the heavy rainfall system. This distribution of PWV suggested that the heavy rainfall might have occurred when this humid air was supplied to the rainfall system.

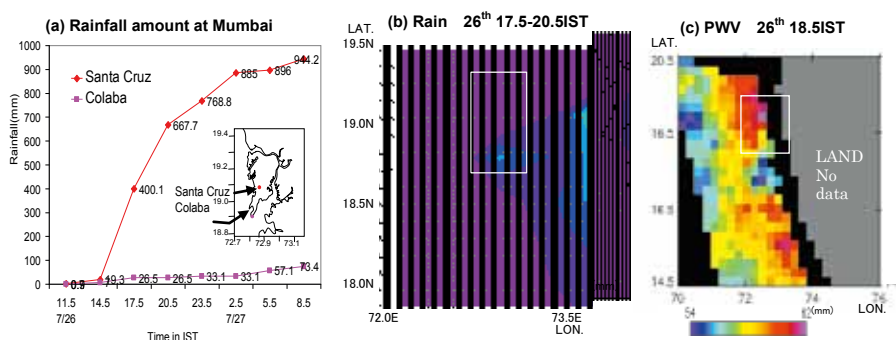


**Fig. C-3-1.** (a) Time series of observed rainfall amount on 26 and 27 July at Santa Cruz and Colaba (After Fig. 1 of Bohra et al. 2005). (b) Three hour rainfall amount estimated by TRMM satellite (After Fig. 2 of Bohra et al. 2005). (c) PWV distribution observed by SSM/I. White rectangles in (b) and (c) indicate the regions of figs. (a) and (b), respectively. After Seko et al. (2008).

<sup>1</sup> H. Seko, S. Hayashi, M.Kunii, and K. Saito

### C-3-2. Design of the downscale experiment

This study used JMA-NHM with triple-nested grids (20 km, 5 km and 1 km). Hereafter, experiments with 20 km will be labeled 20km-NHM (horizontal grid number 200 ×200); those with 5 km will be labeled 5km-NHM (horizontal grid number 400×400); and those with 1 km will be labeled 1km-NHM (horizontal grid number 300×300). Vertically, 40 stretched terrain-following layers were commonly employed in all experiments. The lowest level of the model was located at 20 m, and the top of the model was located at 22.7 km. Initial and boundary conditions of 20km-NHM were obtained from the global analysis data of JMA. Outputs of 20km-NHM and 5km-NHM provided the initial and boundary conditions of 5km-NHM and 1km-NHM. The initial data of 5km-NHM and 1km-NHM were given by the outputs at the forecast time (FT) of 6 hours. Specifically, the initial time of 5km-NHM and 1km-NHM were 11.5 IST and 17.5 IST of 25 July. The forecast period of 20km-NHM, was 36 hours; that of 5km-NHM was 30 hours; and that of 1km-NHM was 9 hours.

### C-3-3. Heavy rainfall reproduced by the downscale experiment

Figure C-3-2a depicts the rainfall distributions from FT = 3 to 27 (hours) produced by 5km-NHM. The rainfall regions were generated along the mountain range near the western coast of India by FT = 3 (14.5 IST). An intense rainfall system was organized near Mumbai by FT = 6 (17.5 IST). The system began to split into several rainfall cells along the mountain range at FT = 18 (5.5 IST, 26 July), and then the intense rainfall was terminated at FT = 23 (10.5 IST, 26 July). The rainfall amount in 17 hours from FT = 6 to FT = 23 caused by the system reached 1,149 mm. The rainfall amount and duration indicated that the heavy rainfall was quantitatively well-simulated.

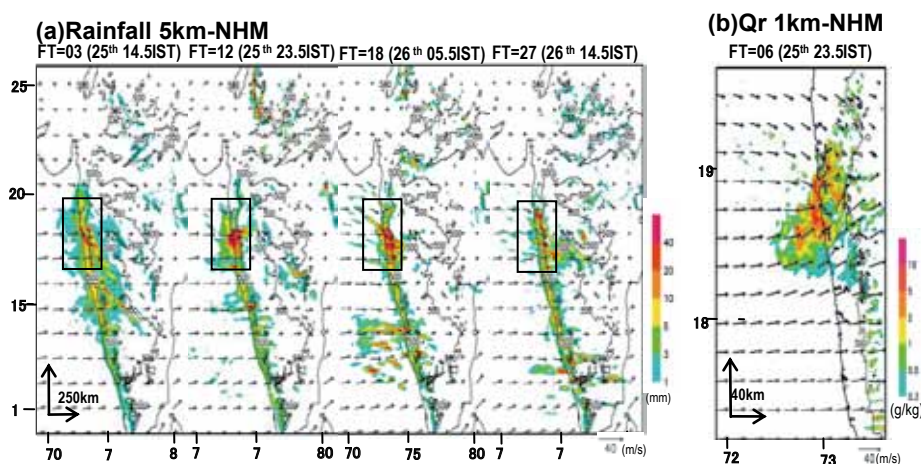


**Fig. C-3-2.** (a) Rainfall distributions from FT=3 to 27 hour by 5km-NHM and (b) horizontal wind and rainwater mixing ratio (Qr) at  $z=0.53$  km at FT=6 by 1km-NHM. Rectangles in (a) indicate the domain of (b). Large arrows in (a) and (b) indicate the horizontal scale of 250 km and 40 km, respectively. After Seko et al. (2008).

Figure C-3-2b depicts the rainwater mixing ratio of the regional rainfall system reproduced by 1km-NHM. The intense rainfall system had already been organized by FT = 6 (23.5 IST) 100 km south of Mumbai. The horizontal scale of regional heavy rainfall was several tens of kilometers. The good agreement of the simulated position and the horizontal scale with observation indicated that

1km-NHM effectively reproduced the regional heavy rainfall. The structure of this intense rainfall system and the factors that produced intense rain were reported by Seko et al. (2008).

#### C-3-4. Heavy rainfall reproduced using LETKF

The factors that caused the heavy rainfall were also investigated by the outputs of the ensemble forecast. In this study, a Local Ensemble Transform Kalman Filter (LETKF) for JMA-NHM (Miyoshi and Aranami 2006) was used. As the forecast models, JMA-NHM with a grid interval of 20 km was used. Size of ensemble member was 20. Initial seed was given by the global analysis of JMA at 00 UTC from 5 to 24 July. The conventional data, such as surface and upper sounding data were assimilated with 6-hours assimilation windows.

Figure C-3-3 shows that rainfall region and water vapor distributions at the heights of 0.5 km and 3 km by the ensemble forecast. Heavy rainfalls near the western coast of India were reproduced in three ensemble members of #006, #007 and #009 among 20 members. Namely, the probability of heavy rainfalls is 15 %.

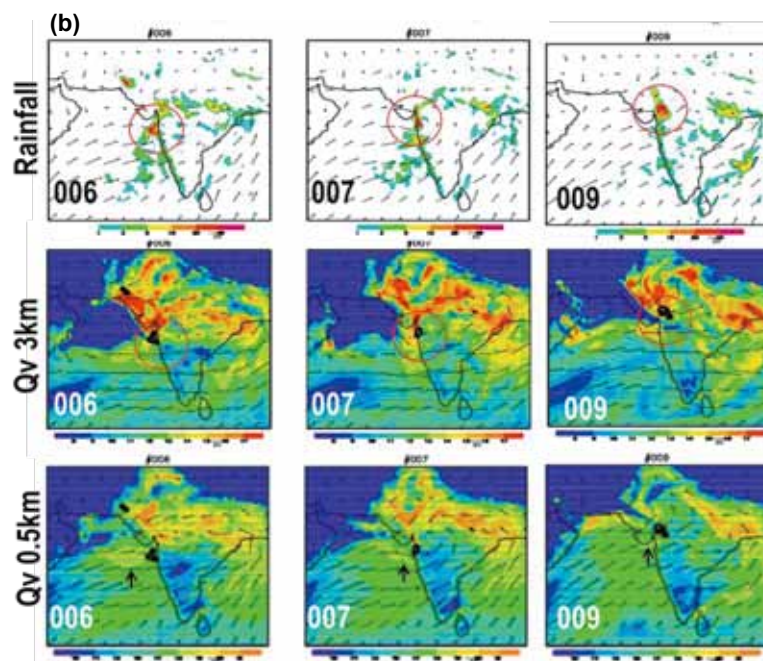


**Fig. C-3-3.** Rainfall and water vapor mixing ratio distributions at the height of 3 km and 0.5 km. Red circles and thick arrows indicate the heavy rainfalls and the low-level airflows that supplies humid air.

Outputs of ensemble members were compared, and then the following features were pointed out as the factors that influence the formation of the heavy rainfall.

- (1) Intense rainfalls were generated at the southern tip of the moist region at the height of 3 km.
- (2) Northerly flows existed in the moist region on the north of intense rainfall.
- (3) Moist air also supplied by the low level westerly flow.
- (4) The humid region at the height of 3 km exists in the inland area in #009. Thus, the orographic effect that produces the thick humid northerly flow was not the indispensable condition for the heavy rainfall formation.

These features indicate that the thick humid airflow from the north and the low-level humid westerly flows are the indispensable factors for the heavy rainfalls. This result is consistent with the observed PWV distribution (Fig. C-3-1c) and the sensitivity experiment's results shown in Seko et al. (2008).

### C-4. Generation mechanisms of convection cells in the tropical region<sup>1</sup>

Because weather systems that cause heavy rainfall are characterized by intense convection cells, generation and development mechanisms of intense convection cells should be understood for disaster mitigation. In mid-latitudes, large-scale convergences such as the Baiu front, meso-scale convergences induced by cold pools, or thermodynamical low-pressure systems have been reported as causes of heavy rainfalls (e.g., Seko et al. 2005; Kawabata et al. 2007). However, convection cells in tropical regions are not as well studied. Because typical atmospheric profiles in tropical regions differ from those in mid-latitudes, some mechanisms, such as gravity waves, might more strongly affect convection cells in tropical regions.

Tropical convection cells were simulated by a high-resolution 2-dimensional nonhydrostatic model by Yamasaki and Seko (1992; abbreviated to YS92 hereafter) to investigate their generation and development mechanisms. They found that convection cells were generated and developed when updrafts resulting from intersecting gravity waves overlapped, or when gravity waves propagated into the humid region. However, YS92 used a 2-dimensional model in which the influence of gravity waves is overestimated when the gravity waves propagate to all directions. To refine the YS92 results, we conducted a reproduction experiment of tropical convection cells using a high-resolution 3-dimensional model. The JMA Climate Data Assimilation System (JCDAS) was used as the realistic initial fields.

#### C-4-1. Ideal experiment with a 2-dimensional model (YS92)

YS92 used a 2-dimensional anelastic model (Yamasaki 1984) with a horizontal grid interval of 1 km. Vertical profiles of temperature and humidity used as the basic fields were those typical of the tropical region (see Table 1 in Yamasaki (1983)). For horizontal winds, a vertical profile with a linear vertical shear of 2 m/km below the height of 3 km was used. The horizontal domain size was set as large as 5000 km, so that factors other than gravity waves (e.g., cold outflow) would not affect the generation of the convection cells. Initial disturbances consisted of two sets of four thermal

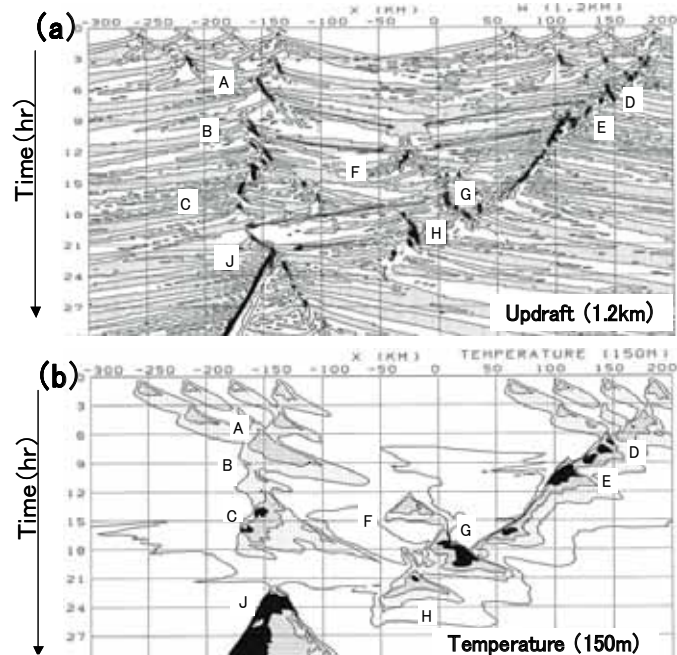


**Fig. C-4-1.** Hovmöller diagrams of (a) updrafts at 1.2km height and (b) temperature at 150 m height. Shaded and dark regions in (a) indicate updrafts and clouds. Arrows indicate the propagations of gravity waves that generate or develop the convection cells F and J. The shaded and dark regions indicate the cold pools produced by the convection cells. After Yamasaki and Seko (1992).

<sup>1</sup> H. Seko, S. Hayashi and K. Saito

bubbles near the center of the model domain. When the numerical integration was conducted, cold outflows and gravity waves that were produced by the initial bubbles triggered successive convection cells.

Figure C-4-1 shows Hovmöller diagrams of updrafts at 1.2 km height and temperature at 150 m height. Updrafts of gravity waves were generated among groups of convection cells and propagated to both directions (Fig. C-4-1a). When updrafts propagated from convection cells A and D, a new convection F was generated between these convection cells, then developed when gravity waves arrived from convection cells B and E. Convection J was generated when gravity waves arrived from convection G and was developed when gravity waves arrived from convection H. We studied the generation and development mechanisms of these convection cells by the vertical distributions of the deviations from their horizontal averages. When gravity waves approached, temperature decreased and relative humidity increased in the updraft region (not shown). Updrafts and these changes caused by gravity waves constituted favorable conditions for the generation and development of new convection cells. There was no cold pool where convection cells F and J were generated (Fig. C-4-1b), which indicates that gravity waves alone can generate and intensify convection cells.

#### C-4-2. Design of experiments

This study reproduced convection cells near Sumatra in the monsoon season. Triple one-way nested downscale experiments were performed so that the horizontal grid interval of the innermost model can produce individual convection cells. The grid intervals of the nested models were 20 km, 5 km, and 1 km, respectively. Initial and boundary conditions of the outer model (20km-NHM) were given by JCDAS (global analysis data by JMA and the Central Research Institute of Electric Power Industry). Thermal bubbles were not replaced in the initial fields. The initial time for the 20km-NHM model was 1200 UTC 28 January 2008, during monsoon season in Southeast Asia. A 6-h forecast of 20km-NHM was used as the initial condition for the second model (5km-NHM), which is enough time for spin-up because convection cells were generated during the first 6 h from the initial time of 5km-NHM. A

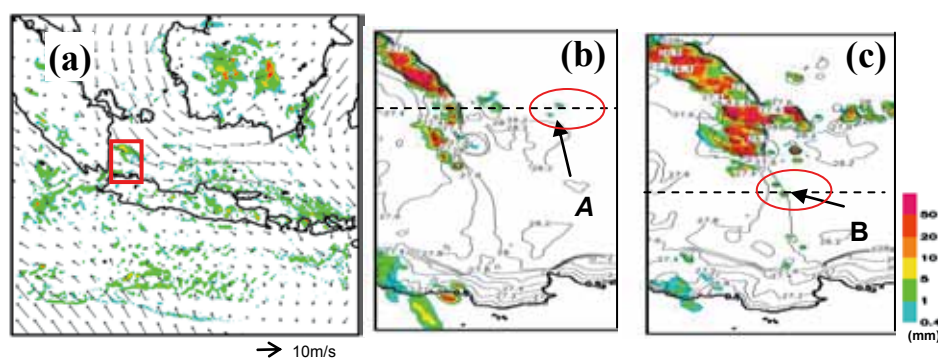


**Fig. C-4-2.** (a) Rainfall regions at 2100 UTC 29 January 2008 reproduced by 5 km-NHM, and at (b) 2230 UTC on 29 and (c) 2320 UTC on 29 reproduced by 1 km-NHM. Initial time of 5km-NHM and 1km-NHM are 1800 UTC 28 and 1500 UTC 29, respectively. Contours in (b) and (c) indicate the temperature at 1000 hPa. Red rectangular in (a) indicates the regions of (b) and (c).

21-h forecast of 5km-NHM was used as the initial condition for 1km-NHM. The time lag between the initial times of 5km-NHM and 1km-NHM (21 h) was determined by the generation time of convection cells, not by the spin-up time. The Kain-Fritsch convective parameterization scheme was adopted in 20km-NHM and 5km-NHM. The bulk method which predicts cloud water, rainwater, cloud ice, snow, and graupel was adopted as the microphysical process for 1km-NHM.

### C-4-3. Generation mechanisms of convection cells by gravity waves

Figure C-4-2a shows the 1-h rainfall and surface horizontal wind distribution at 2100 UTC on 29 January 2008 reproduced by 5km-NHM. On the eastern side of Sumatra, west-northwesterly and northwesterly flow converged and a rainfall region was generated there.

Figures C-4-2b and c show the 1-h rainfall and surface temperature distributions reproduced by 1km-NHM. The intense rainfall band extending southeastward on the eastern side of Sumatra corresponds to the rainfall region in Fig. C-4-2a. Small convection cells A and B were generated on the eastern side of the convective band at 2230 UTC and on the southern side at 2320 UTC. Contours near the convection cells A and B in Figures C-4-2b and c show that an intense cold pool did not exist around them. We chose these two events as the targets of this study because they were not generated by an intense cold pool.

#### (a) Convection cells generated along the convergence zone

Convection cells A were generated where the temperature gradient was weak. Figure C-4-3 shows Hovmöller diagrams of updrafts at two levels as well as rainfall, temperature, and dew-point deficits ( $T - T_d$ ) across convection cells A.

Convection cells were generated repeatedly after the propagation of the weak updraft region at 925 hPa from the west (indicated by arrows in Fig. C-4-3c). These weak updrafts were produced by the convergence of the west-northwesterly and northwesterly flow, shown in Figure C-4-2a. Convection cells A were generated far from other convection cells when the updrafts at 925 hPa (Fig. C-4-3c) and 850 hPa, which propagated from the east (arrow in Fig. C-4-3a), overlapped. The contours of temperature and dew-point deficit at 850 hPa show

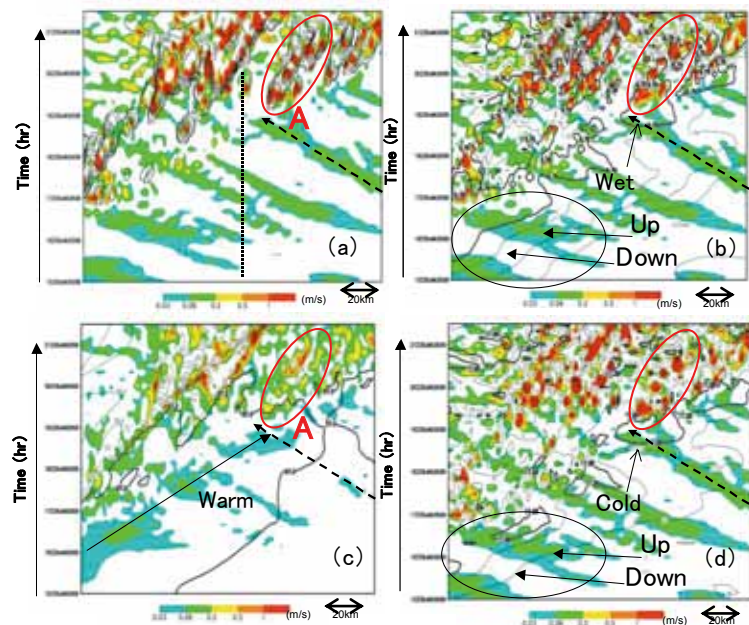


**Fig. C-4-3.** Hovmöller diagrams of updrafts (colored region) at (a~b, d) P=850hPa and (c) 925 hPa along the broken line in Fig. C-4-2(b). Contours in (a)~(d) indicate (a) rainfall, (b) dew-point deficit at P=850hPa, (c) temperature at P=1000hPa and (d) temperature at P=850hPa, respectively.

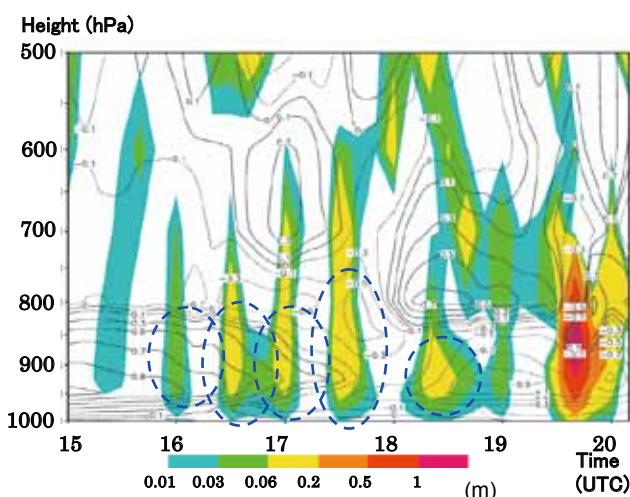
that both parameters decreased rapidly as the updrafts passed (Figs. C-4-3d and b). These variations show that the updrafts were induced by gravity waves. Before the generation of convection A, the temperature became lower and the dew-point deficit became smaller than before the arrival of the gravity waves (Figs. C-4-3d and b). These changes favored the generation and development of convection cells, and they are common to convection cells created in the 2-dimensional model of YS92. Temperature at 1000 hPa in Figure C-4-3c shows that a cold pool did not exist and could not have generated the convection cells.

Figure C-4-4 is a time-height diagram of the updraft and deviation of temperature from the temporal average. Temperature below 800 hPa decreased with time, caused by the convergence of west-northwesterly and northwesterly flows. The updrafts below 700 hPa appeared at 30–60 min intervals. As shown in Figure C-4-3, temperature rapidly decreased when the updraft passed. The extent of these variations was limited below 700 hPa, which we attribute to the large vertical gradients of potential temperature (5.5 K/km) at the height of 2–3 km at the initial time of the 1km-NHM model over the Java Sea. Low-equivalent potential temperature air at the middle level (500 hPa) has been reported as the factor causing heavy rainfalls in middle latitudes (e.g., Kato and Aranami 2005). However, the height at which this factor was effective in the generation and development of convection cells in this study was 800–900 hPa. The origin of the gravity waves that propagated to A, investigated by tracing back the pattern of horizontal distribution of vertical velocities at 850 hPa, was around the weak rainfall regions that were developed in the Java Sea from 0200 to 0700 UTC 29 January.

### (b) Convection cells generated along the edge of the weak cold pool

On the southern side of the convective band east of Sumatra, a weak cold region moved eastward (Fig. C-4-2c). The drop of temperature was as small as 0.2 °C. Convection cells B were generated at the leading edge of this cold pool.

Figure C-4-5 shows Hovmöller diagrams across convection B. Figure C-4-5c shows that the cold pool (colder than 27.0 °C) extended eastward and that the weak updraft was produced at its leading edge. At 950 hPa, above the extent of the updraft caused by the cold pool, another updraft propagated from the west (indicated by the dashed arrow in Fig. C-4-5a). The propagation speed of this updraft was much greater than the speed of expansion of the cold pool, indicating that the updraft was induced by gravity waves. When the gravity waves propagating from the west reached the leading



**Fig. C-4-4.** Time-height diagram of updraft (colored region) and deviation of temperature from temporal average (contours) along the dotted line of Fig. C-4-3(a).

edge of the cold pool, the temperature decreased and the dew-point deficit became smaller (Figs. C-4-5a and d) and convection cells B were then generated. This sequence of events was similar to, but slower than, the events in the case of convection cells A.

**C-4-4. Summary**

We used convection cells reproduced from the analyzed fields by the high-resolution 3-dimensional nonhydrostatic model to investigate the generation and development mechanisms of convection cells in the tropical region. The results are summarized as follows:

- (1) Updrafts from low-level gravity waves made the lower atmosphere cooler and moister and may trigger the generation of convection cells.
- (2) When updrafts from low-level gravity waves overlapped with other weak updrafts caused by large-scale convergence or weak cold pools, convection cells were generated. Low-level gravity waves can generate or develop new convection cells if other weak updrafts exist. This result means that the origin and timing of convection cells are influenced by gravity waves.
- (3) These results are consistent with those of YS92.

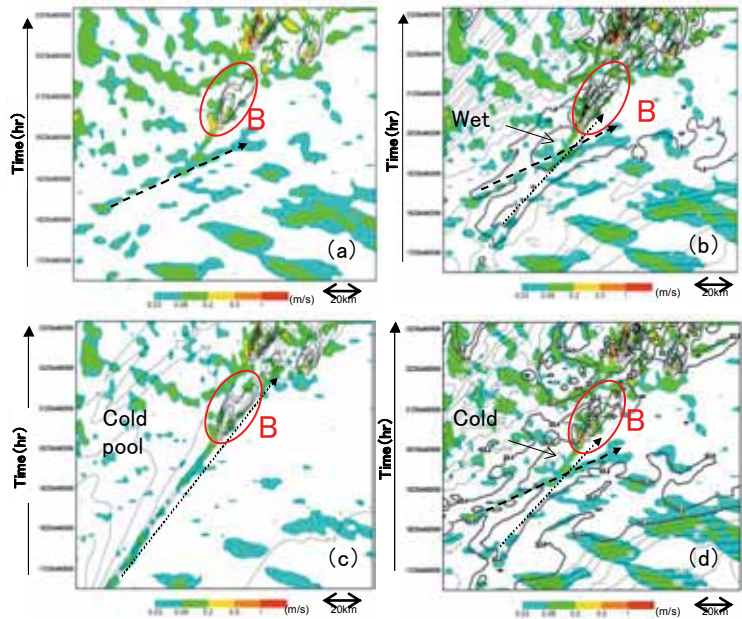


**Fig. C-4-5.** Hovmöller diagrams of updrafts (colored region) at (a,b and d) P=950 hPa and (c) 975hPa along the broken line in Fig. C-4-2(c), (a) rainfall (b) dew-point deficit at P=950hPa, (c) temperature at P=1000hPa and (d) temperature at P=950hPa.

## **C-5. Tests of cumulus schemes in JMA-NHM over Southeast Asia<sup>1</sup>**

The JMA nonhydrostatic model (NHM) was implemented in Southeast Asia in short-term forecasts of up to 18 h over one year with 25 km horizontal resolution. Three cumulus schemes were tested in the model: Kain-Fritsch, Grell and Arakawa-Schubert. Diagnosis of bias and correlation coefficients of rainfall shows that the Grell scheme performed the best and Arakawa-Schubert performed the worst.

### **C-5-1. Introduction**

NHM (Saito et al. 2006) is an operational weather forecast model developed originally for applications in Japan. To adapt it to weather forecasting in Southeast Asia, we first need to verify its performance in tropical regions. We conducted experiments using three cumulus schemes (Kain-Fritsch, Grell, and Arakawa-Schubert) in NHM to identify which scheme is more suitable to forecast weather in Southeast Asia.

### **C-5-2. Experimental Design**

We integrated JMA-NHM version 2010-May-10 for one year from 0000 UTC 1 January to 2300 UTC 31 December 2004. Because neither El Niño nor La Niña occurred in this year, modeling errors associated with these inter-annual anomalies should be small in the experimental period. We conducted three experiments in which the cumulus scheme was respectively Kain-Fritsch (tuned for Japan region, Saito et al. 2006), Grell, and Arakawa-Shubert. Because neither data assimilation nor Spectral Boundary Coupling (SBC, e.g., Kida et al. 1991) were used, we only examined experiments initialized at 0000 and 1200 UTC with short-term forecasts (e.g., Hayashi et al. 2008) of 18 h where the first 6 h were discarded as model spin-up.

The model resolutions were 25 km horizontally and 40 layers vertically and the grid size is 160×120 points with the domain center at lat 4°N, long 110°E. The time step is set to be 75 s. We used Japan 25-year Re-Analysis data (JRA25) as initial and boundary conditions.

### **C-5-3. Results**

To verify the results of the NHM simulations, we compared rainfall amounts from the model with satellite-derived data from Tropical Rainfall Measurement Mission (TRMM) version 3B42. This was because the conventional weather observation network in Southeast Asia is too sparse to capture mesoscale convective systems at time-scales of hours (Koh and Teo 2009).

Statistical verification was carried out based on measures such as bias and correlation. Use of root-mean-square error (RMSE) was avoided as it depends more on the ambient variability of the weather rather than on the model error itself (Koh and Ng 2009).

Figure C-5-1 shows the annual mean rainfall of TRMM satellite data and the bias in rainfall (NHM minus TRMM) under the three cumulus schemes. The distribution of rainfall in TRMM data shows that rainfall concentrated over land areas such as Borneo, the Malay Peninsula, and Sumatra. NHM

---

<sup>1</sup> S. Koseki and T.-Y. Koh

underestimated precipitation over land with all three schemes. In particular, underestimation of rainfall was greatest around the northwestern coast of Borneo (lat 2°N to 4°N, long 110°E to 114°E). Although the performances of Kain-Fritsch and Grell were identical over land, the Grell scheme showed the best bias performance of the three schemes, because its underestimation of rainfall was relatively small, especially over the sea. The Arakawa-Schubert scheme was worse than the other two schemes. In contrast, NHM overestimated precipitation in inland Borneo, along the southern coast of Sumatra, and over Sulawesi. These overestimations arose partly from a strong sensitivity of rainfall to model topography, as seen in other models (Teo et al. 2011). Another reason is that the diurnal cycle in the study area may not be reproduced sufficiently. Rainfall here is manifested basically in features of the diurnal cycle, such as sea/land breeze circulation.

Figure C-5-2 shows diagrams of monthly correlation coefficients between NHM ( $N$ ) and TRMM ( $T$ ),  $r = \frac{\text{cov}(N, T)}{\sqrt{\text{var}(N) * \text{var}(T)}}$  for the area-averaged rainfall in six regions: the Malay Peninsula, inland Borneo, coastal Borneo, southern Sumatra, the South China Sea, and the Java Sea. Note that there is some uncertainty in the correlation values associated with comparing 3-hourly time series snapshots of rainfall in RMM and NHM accumulated rainfall. The Kain-Fritsch and Grell schemes generally showed better performance than the Arakawa-Shubert scheme in all six areas. As the weather patterns in this region tend to be dominated by a strong diurnal cycle of land-sea breeze circulation (Joseph et al. 2008), the correlation coefficients are indicative of how well the model captures the underlying mesoscale dynamics.

#### **C-5-4. Summary**

We conducted test experiments of three cumulus schemes in NHM for Southeast Asia. The Grell scheme showed the best performance in short-term forecasts because its bias was smaller than those of the other two schemes. The correlation coefficient for the Grell scheme was comparable to that of the Kain-Fritsch scheme but better than that of the Arakawa-Shubert schemes, which was the worst of three.

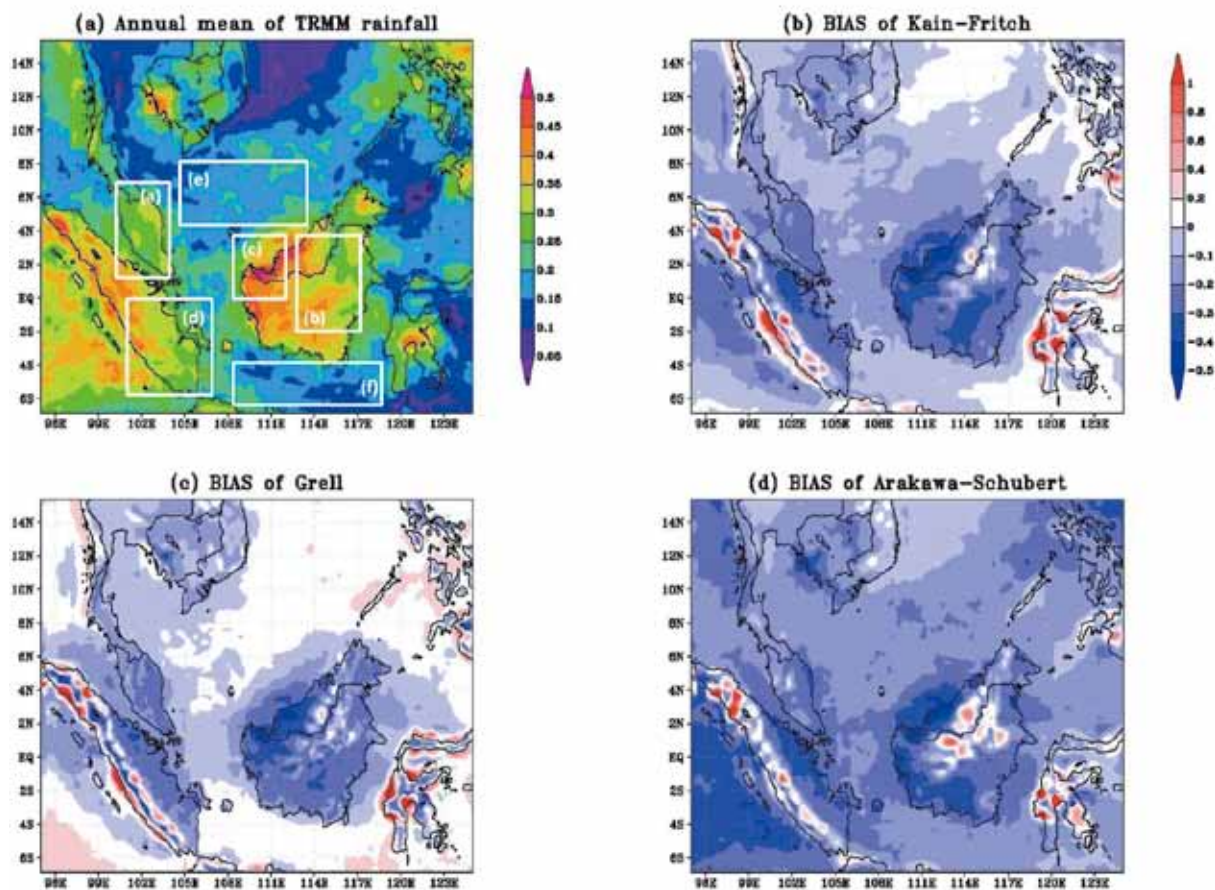


**Fig. C-5-1.** (a) Annual mean of TRMM rainfall (mm/hr) in 2004. Rectangles are areas where rainfall is averaged in Figure C-5-2. (b)-(d) NHM minus TRMM annual mean rainfall (mm/hr) with the Kain-Fritsch (b), Grell (c), and Arakawa-Schubert scheme (d).

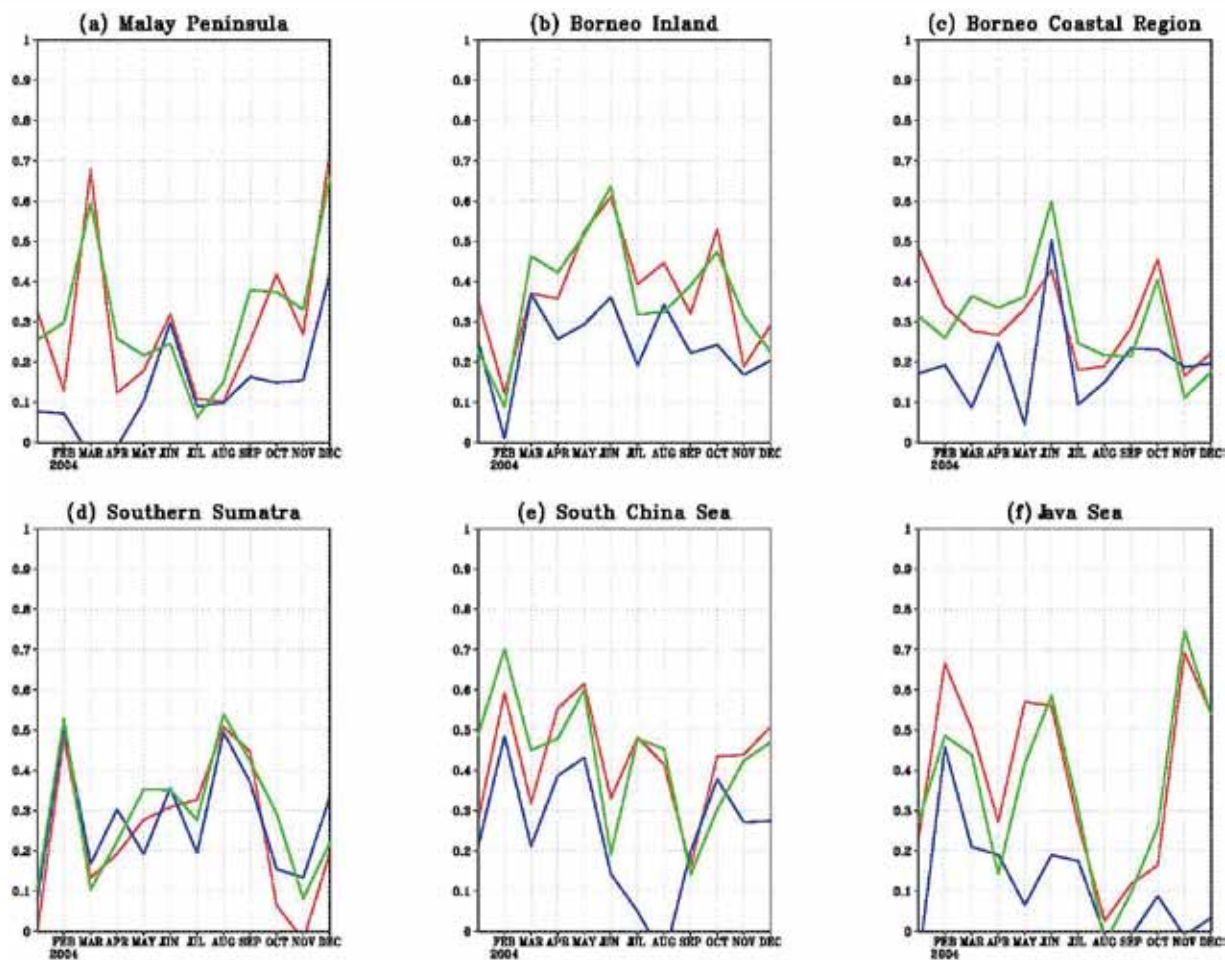


**Fig. C-5-2.** Monthly correlation coefficients of 3-hourly rainfall between NHM with three schemes and TRMM averaged over the rectangular areas in Figure C-5-1. Red denotes Kain-Fritsch, green denotes Grell and blue denotes Arakawa-Schubert scheme.

## **C-6. Model verification of HRM, NHM, WRF-ARW, and WRF-NMM in predicting precipitation<sup>1</sup>**

### **C-6-1. Introduction**

Numerical weather predictions have been conducted at Vietnam National University of Hanoi (VNU) since 2000 with a mesoscale hydrostatic model named HRM (Majewski, 2009), the former operational limited-area model of the German Weather Service (DWD) that is run at VNU with DWD's permission. With the general shift to nonhydrostatic models, in 2004 VNU started deploying the MM5 model, then the WRF models WRF-ARW (Skamarock et al. 2008) and WRF-NMM (Janjic et al. 2010). When VNU joined the research project "International Research for Prevention and Mitigation of Meteorological Disasters in Southeast Asia," the Meteorological Research Institute of Japan (MRI) provided VNU with a research license for NHM (Saito et al. 2007).

In Vietnam, tropical cyclones and heavy rainfall are the two most severe meteorological disasters. Although VNU uses many models in research, only HRM was applied in forecasting these two events after it was verified for more than two years. Other models were used only for case studies. WRF has shown better performance than HRM in some of these cases, but not in others. To apply a new model for forecasting severe weather phenomena, we need to document its superior skill through a formal comparison (e.g., Hayashi et al. 2008; Chan et al. 2010) with HRM forecasts.

This report documents a performance intercomparison among the four models HRM, NHM, WRF-ARW, and WRF-NMM. Of these models, only HRM is hydrostatic, although the others support hydrostatic options. Our study target was the precipitation forecast for Vietnam in September 2009. This effort was part of a verification project that assesses the performance of all models running in research institutes and operational centers in Vietnam.

### **C-6-2. Data and method**

Because the four models differ in dynamics, physics, and numerical features, it was impossible to use identical configurations for all models. However, we used the same settings for initial and boundary conditions, domains, and resolutions.

First, all models used the same initial and boundary conditions from the Global Forecast System (GFS) analyses and forecasts with a resolution of  $0.5^\circ$ . The boundary condition update interval was 3 h. The sea-surface temperature fields were also taken from the GFS analyses. The constant fields such as topography, land use, and vegetation fraction were derived from the United States Geological Survey (USGS) dataset.

Second, the domain and resolution were nearly the same for all models. NHM and WRF-ARW use Mercator projection, HRM uses regular latitude/longitude projection, and WRF-NMM uses rotated latitude/longitude projection. Figure C-6-1 shows the HRM domain with  $201 \times 161$  grid points; the other models also included this domain but were not limited to it. The resolution of this domain is  $0.15^\circ$ . NHM and WRF-ARW set that resolution to 17 km, which is identical to  $0.15^\circ$  at the equator. Because of its special grid type (Arakawa E), the WRF-NMM resolution was set to  $0.11^\circ$ , which is

---

<sup>1</sup> L. Duc and K. T. Xin

nearly  $0.15^\circ$  when multiplied by  $\sqrt{2}$ . All models had 30 vertical layers.

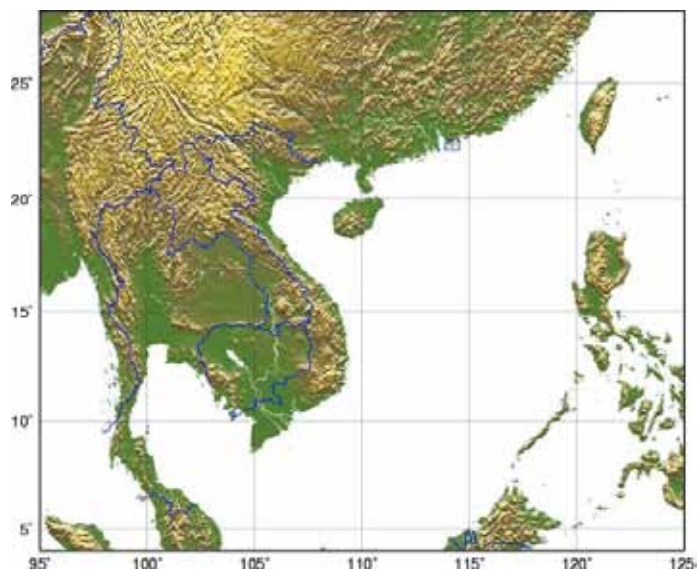


**Fig. C-6-1.** HRM domain.

The models were targeted to the period September 2009. In this period, tropical cyclones Mujigae and Ketsana hit coastal areas of Vietnam and tropical cyclone Koppu affected all of Vietnam. All models were run out to 48 h. Although the spatial resolutions were nearly the same, the time steps were different. The time steps and other different features are listed in Table C-6-1.

**Table C-6-1.** Model configurations.

Model	HRM	NHM	WRF-ARW	WRF-NMM
Version	2.4	2008	3.0.1	3.0.1
Time step	90s	40s	90s	40s
Radiation	Ritter and Geleyn scheme	GSM0412	RRTM + Duhia	GFDL
Cumulus parameterization	Tiedtke	Modified Kain-Fritsch	Kain-Fritsch	Betts-Miller-Janjic
Microphysics	Doms and Schattler scheme	6-class	WSM 3-class scheme	Ferrier scheme
Boundary layer	Mellor-Yamada Level 2	Improved Mellor-Yamada Level 3	Yonsei University scheme	Mellor-Yamada-Janjic TKE
Soil model	Heise and Schrodin 7-layer scheme	Thermal diffusion 4-layer scheme	4-layer Noah LSM	4-layer NMM LSM

Precipitation verifications were conducted using ground observations. There are about 400 rain gauges yielding an average resolution of 28 km over Vietnam. As Cherubini et al. (2002) pointed out, for matching spatial scales, upscaled observations should be used instead of point observations such as SYNOP stations; thus, verification on the model space was adopted. The three-pass Barnes scheme (Achtmeier, 1989) was used to upscale rain gauge data into a regular latitude/longitude grid that is a subdomain of the HRM domain covering Vietnam. Precipitation forecasts from the four models were mapped to the observation grid using interpolation to the nearest grid point. Because all models have nearly similar domains and resolutions, this strategy did not distort rainfall patterns or spread out rain fields.

### C-6-3. Results

The total accumulated 24-h (first day) rainfall forecasts in September 2009 are shown in Figure C-6-2 along with rainfall observations. The rainfall pattern was well forecasted by HRM. NHM and WRF-NMM also represented this pattern, but these two models underestimated the rainfall amount. WRF-ARW showed a false alarm area south of the rainfall peak in central Vietnam.

The bias and equitable threat scores (ETS) against rainfall thresholds (Fig. C-6-3) show that WRF-ARW overestimated and HRM and NHM underestimated precipitation at all thresholds. NHM bias scores were higher than those for HRM. The WRF-NMM bias score decreased rapidly with rainfall thresholds, indicating that the model predicted more light rain and less heavy rain than observations. In terms of ETSs, WRF-NMM is the worst model and HRM is the best one. However, for thresholds less than 20 mm/day, HRM, NHM, and WRF-ARW have the same performance. HRM only beats other models for heavy rains with thresholds exceeding 25 mm/day.

Figures C-6-4 and C-6-5 show results for forecasts in the range of 24–48 h (second day). Second-day forecasts were much like those for the first-day forecasts, with some minor differences. HRM is still the best model and WRF-NMM the worst, although ETS values were less than those for the first-day forecasts. The underestimation of HRM and NHM was the same; however, the HRM bias was closer to 1 than the NHM bias, the reverse of the situation for the first-day forecasts.

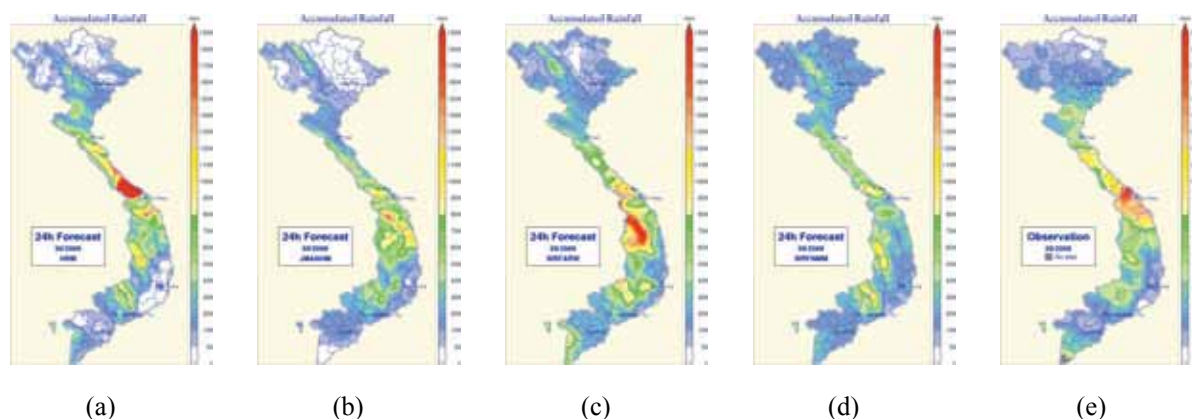


**Fig. C-6-2.** Total accumulated rainfalls in 09/2009 as forecasted by (a) HRM, (b) NHM, (c) WRF-ARW and (d) WRF-NMM for the first day and (e) observation.

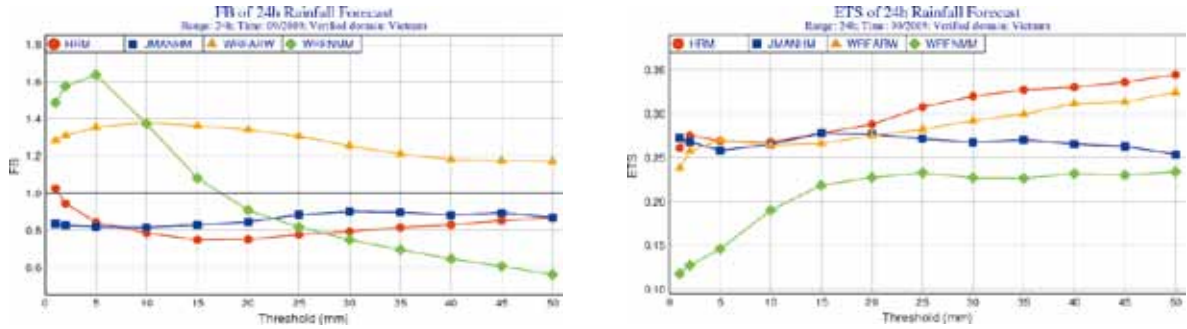


Fig. C-6-3. Bias and equitable threat scores for the first day rainfall forecasts from HRM, NHM, WRF-ARW and WRF-NMM.

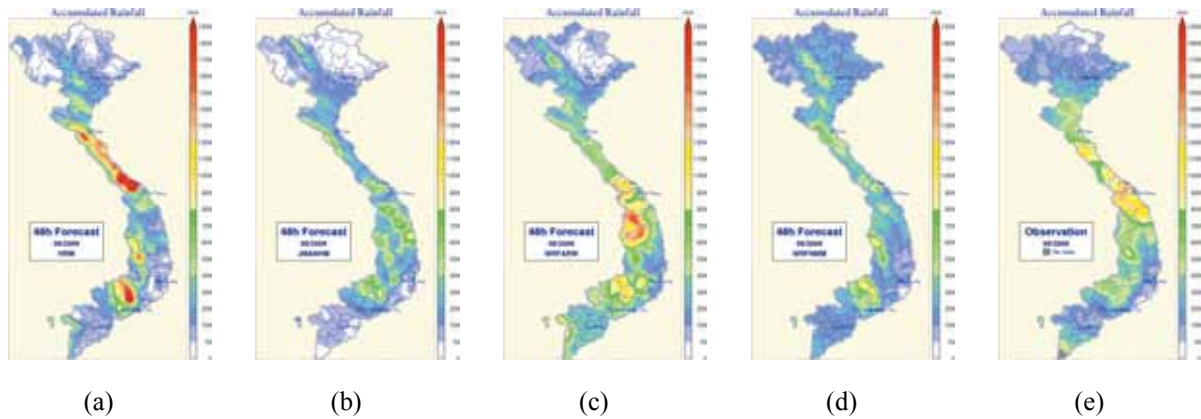


Fig. C-6-4. The same as Fig. C-6-2 except for the second day forecasts.

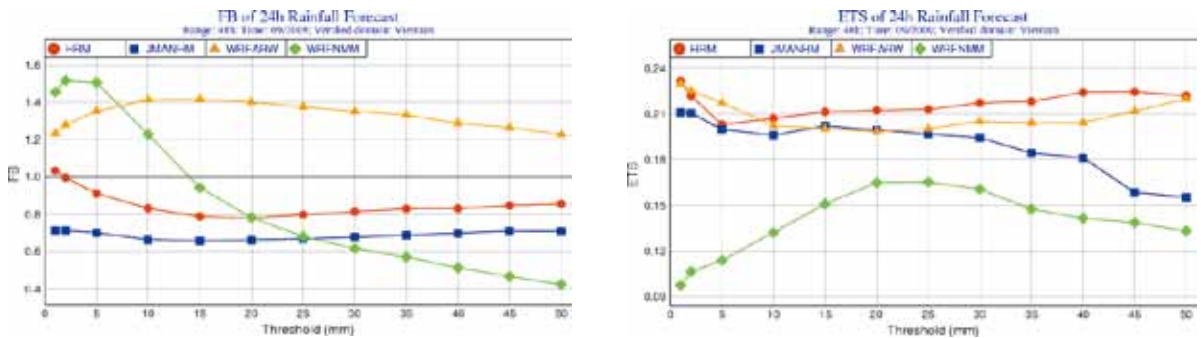


Fig. C-6-5. The same as Fig. C-6-3 except for the second day forecasts.

**C-6-4. Conclusion**

We compared the performance in precipitation forecasts from the four models HRM, NHM, WRF-ARW, and WRF-NMM using GFS analyses and forecasts as initial and boundary conditions, respectively. The resolutions were almost the same, approximately 0.15°. Differing model projections made the domains for each model different, but domains were chosen to minimize the impact of different domains on forecasts. The period of September 2009 was selected, when three tropical cyclones affected Vietnam.

The forecasts were verified against rain gauge data over Vietnam. In the first step, all observations were mapped to an analysis grid covering Vietnam at a resolution of 0.15° by the three-pass Barnes

scheme. For the next step, rainfall forecasts were interpolated to the analysis grid by the nearest point method. Then, verification was done on the analysis grid.

The results highlighted HRM as the best model and WRF-NMM as the worst. HRM tended to underestimate precipitation, as did NHM. WRF-ARW overestimated precipitation for the whole range of rainfall thresholds. Models HRM, NHM, and WRF-ARW exhibited similar performances for light and moderate rains. HRM was the best at predicting heavy rainfall.

The most interesting result is that the performance of a hydrostatic model (HRM) was better than those of nonhydrostatic models. However, at  $0.15^\circ$  resolution, the difference was small. To have a fair comparison, a higher resolution experiment ( $0.04^\circ$  or  $0.05^\circ$ ) should be conducted. As a hydrostatic model, HRM is only adequate for resolutions lower than 7 km. In this case, HRM must be excluded from the comparison. In a tropical region like Vietnam, convective processes have an important role in generating precipitation. Using high-resolution models will improve forecasts for convective rains.

We note that none of the models in this experiment was adapted for tropical regions; they were all developed and first applied in extratropical countries. NHM underestimated the diurnal change of surface temperatures, which we attribute to the inappropriate application of the nonlinear computational diffusion to the number concentration of cloud ice (see Section C-2-5).

## **C-7. A Numerical Experiment on the Heavy Precipitation during the Jakarta Flood Event in January-February 2007<sup>1</sup>**

### **C-7-1. Introduction**

A devastated flood event had occurred at Jakarta on February 2007, which was mainly due to heavy rainfall for several times from 31 January to 2 February. According to the Indonesian Meteorological, Climatological, and Geophysical Agency (BMKG) report, the highest daily rainfall was 340 mm, which was measured on 2 February at Pondok Betung Station (6.2°S, 106.6°E). Torrential rains that repeatedly occurred over West Java coincided with a strong and persistent trans-equatorial monsoon surge from the Northern Hemisphere (Wu et al. 2007). The strong monsoon flow near the surface and the upper southeasterly wind over it produced a low-level vertical shear of winds. The shear with wet lower and dry middle layers allowed the severe moist convections to develop repeatedly.

In this study, a time-lagged ensemble forecast (e.g., Branković et al. 1990) is performed for the two-month period including the Jakarta Flood event with a regional model which consists of a single domain with a relatively coarse resolution. Based on the ensemble forecast data, we investigate the temporal modulation of precipitation and three-dimensional synoptic fields in the periods before, during, and after the heavy rainfall in Jakarta in 2007.

### **C-7-2. Numerical Experimental design**

The numerical model used in this study is Japan Meteorological Agency - non-hydrostatic model (NHM; Saito et al. 2006, 2007). We set up a single computational domain with a 20-km horizontal resolution. The domain has  $103 \times 115$  grid points centered at 5°S, 110°E on a Mercator projection. The topography of the domain is presented in Fig. C-7-1. The subgrid scale parameterization schemes and parameter settings that we employ are the same as those of Hayashi et al. (2008) with their recommended values tuned for the 20-km horizontal resolution. The cumulus parameterization scheme is a modified Kain-Fritsch. The cloud microphysics scheme is a 6-class bulk microphysics with prediction of number concentration of ice particles. The GSM0412 radiation scheme (Yabu et al. 2005) and an improved Mellor-Yamada Level 3 planetary boundary layer scheme (Nakanishi and Niino 2004, 2006) are used. The National Centers for Environmental Prediction Global Tropospheric Analyses (final analyses) with the horizontal resolution of  $1^\circ \times 1^\circ$  and the time interval of six hours are used for the model input.

To run the time-lagged ensemble forecast, we follow the same procedure and method used by Mittermaier (2007), except for the length of individual forecast. We perform 72-hour forecasts every 6 hours, and exclude the initial 18 hours for analysis to avoid the effect of unrealistic convections in the spinup processes. Thus, the number of ensemble members becomes nine. We analyze the two-month period (twelve pentads) from 0000 UTC 1 January to 2300 UTC 1 March 2007. We use Tropical

---

<sup>1</sup> N.J. Trilaksono, S. Otsuka, and S. Yoden

Rainfall Measuring Mission (TRMM) 3B42 (Huffman et al. 2007) as comparison data with the model output.

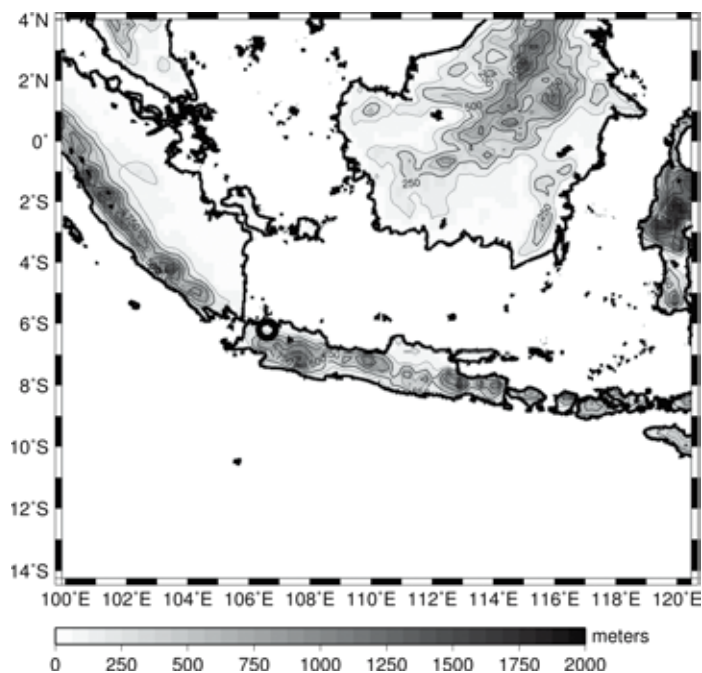


**Fig. C-7-1.** The model domain of computation. Shading and contours show topography (m) of the domain. The open circle denotes the location of Pondok Betung Station. ‘After Trilaksono et al. (2011)’ with some modifications.

### C-7-3. Results of the experiment

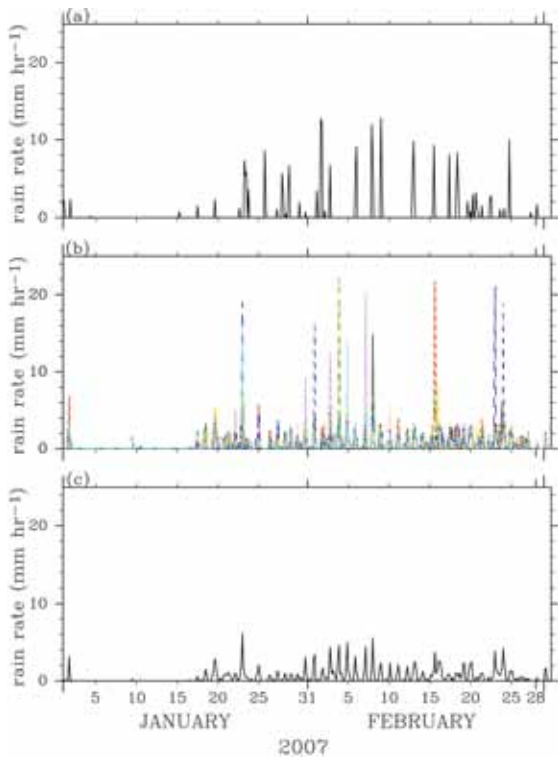
Figure C-7-2 shows the time series of (a) the TRMM estimated rainfall, (b) the model simulated precipitation rate of the nine ensemble members, and (c) their ensemble mean in the unit of  $\text{mm hr}^{-1}$  at the nearest data point to the Pondok Betung Station for the two-month period. The location of Pondok Betung is denoted by the open circle in Fig. C-7-1. The characteristic time scale of the precipitation rate is generally small (less than one day) suggesting a convective origin, as shown by the TRMM data (Fig. C-7-2a). This feature of convective precipitation is well reproduced in the model. Some ensemble members show heavy precipitation ( $> 10 \text{ mm hr}^{-1}$ ) during or just after the period of Jakarta Flood event (Fig. C-7-2b). Such enhancement of precipitation is also discernible in ensemble average (Fig. C-7-2c), although the magnitude is much smaller. Both the TRMM data and the model results show modulation of precipitation rate in the two-month period. There is little rainfall observed during the first half of January, whereas rainfall occurs frequently afterward.

Figure C-7-3 shows the time-latitude cross sections of (a) the TRMM estimated rainfall data and (b) the ensemble mean of the model simulated precipitation rate averaged between  $105.5^\circ\text{E} - 108.5^\circ\text{E}$ . The horizontal lines in Figs. C-7-3a and b denote the latitude of  $6.2^\circ\text{S}$ , which is the latitude of Pondok Betung Station in the northern part of Java Island. The TRMM data (Fig. C-7-3a) shows that in the first half of January, continual precipitation exists between  $2^\circ\text{S}$  and  $5^\circ\text{S}$ , whereas intermittent rainfall with an interval of about one week exists to the north of  $2^\circ\text{S}$ .

There is little rain to the south of  $5^\circ\text{S}$  during the period. The meridional extent of heavy rainfall occurrence varies after around 17 January. Before the Jakarta Flood event, a signal of heavy rainfall propagates from  $4^\circ\text{N}$  around 25 January to  $6^\circ\text{S}$  around 30 January. After the signal reaches the

northern part of Java Island, it does not propagate any farther. The meridional extent of rainfall concentrates in the latitude between 5°S and 8°S from around 30 January to 15 February. Right after 15 February, it becomes larger with higher rain rate to the south of 6°S.

The ensemble mean of the model output precipitation rates (Fig. C-7-3b) resembles that of the TRMM data. The north-south contrast of precipitation before around 17 January is reproduced well in the model. Propagation of a signal of heavy rainfall just before the Jakarta Flood event is also reproduced well. The meridional extent of precipitation is somewhat larger in the ensemble mean from 31 January to 8 February. Modulation of intermittent precipitation to the south of 6°S in the second half of February is also reproduced well.



**Fig. C-7-2.** Time series of (a) the TRMM estimated rainfall, (b) the model simulated precipitation rate of the nine ensemble members, and (c) their ensemble mean in the unit of  $\text{mm hr}^{-1}$  at the nearest points to the Pondok Betung Station for the two-month period from 0000 UTC 1 January to 2300 UTC 1 March 2007. The location of Pondok Betung station is denoted by the open circle in Fig. C-7-1. ‘After Trilaksono et al. (2011).’

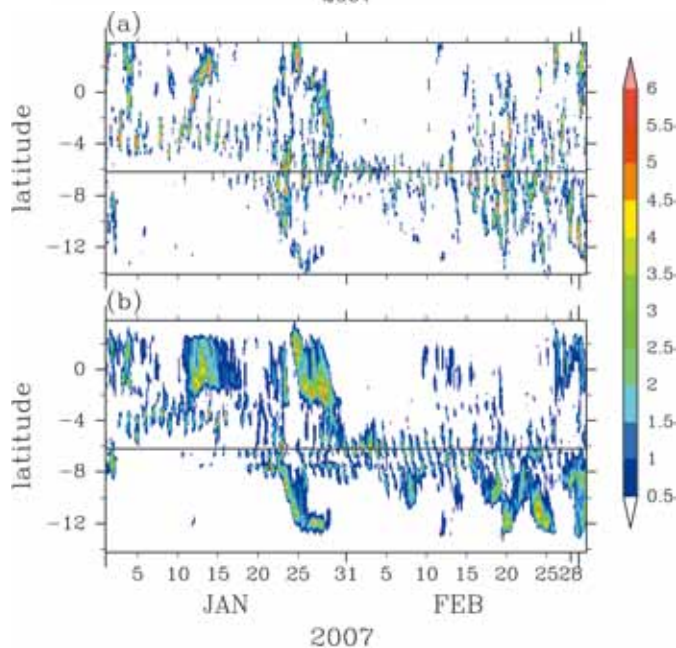


**Fig. C-7-3.** Time-latitude cross sections of (a) the TRMM data and (b) the ensemble mean of the model simulated precipitation rate averaged between 105.5°E – 108.5°E. The horizontal lines in (a) and (b) denote the latitude of 6.2°S which is the latitude of Pondok Betung station. ‘After Trilaksono et al. (2011).’

Figure C-7-4a shows the time-latitude cross section of the ensemble mean of the model simulated meridional wind anomaly. It shows that there is positive (northward) wind anomaly in most of the latitudes in the first 20 days of January. Propagation of a signal of negative anomaly of the meridional winds is evident from 4°N on 27 January to 6°S on 29 January, which corresponds to the propagation of a signal of precipitation in Fig. C-7-3. The negative anomaly of meridional winds continues about one week at 6°S during and after the Jakarta Flood event. Another event of the propagation of negative meridional wind anomaly is seen from 4°N on 22 January to 14°S on 24 January with some correspondence to the enhancement of precipitation shown in Fig. C-7-3b.

A cold anomaly persists from 29 January to 4 February during and after the Jakarta Flood event around 6°S (Fig. C-7-4b). It is related to the cold anomaly propagation from the north associated with the propagation of negative meridional wind anomaly before the initial date as described above. The association of the cold anomaly with the northerly anomaly is indicative of a cold surge event. Continuation of the cold surge reaches 12°S on 29 January and the south end of the computational domain on 3 February. Note that there is no evidence of the cold anomaly around 22 January that corresponds to the strong negative meridional wind anomaly. This is a surge event but not a cold surge event. Larger variability of temperature anomaly exists to the south of Java Island for the two-month period, in which cold (warm) anomaly dominates during January (February).

Time-latitude variations of relative humidity (Fig. C-7-4c) shows similar pattern with those of the precipitation shown in Fig. C-7-3b. The period of late January to early February is also marked by a moist condition near the surface (at 850 hPa) with value of relative humidity exceeding 96% over the northern part of Java Island.

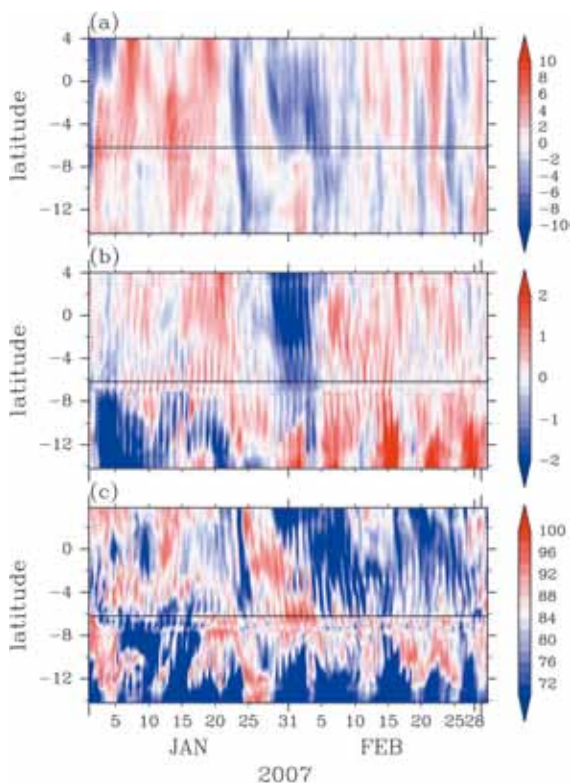


**Fig. C-7-4.** Same as Fig. C-7-3 except for the ensemble mean of the model simulated (a) meridional wind anomaly ( $\text{m s}^{-1}$ ), (b) temperature anomaly ( $^{\circ}\text{C}$ ), and (c) relative humidity (%) at 850 hPa. Here, we define an anomaly as a deviation from the two-month average. ‘After Trilaksono et al. (2011).’

Figure C-7-5 shows the horizontal distributions of the ensemble mean of the model simulated precipitation rate (shades) and horizontal winds at 850 hPa (arrows) averaged for each pentad. Here, we only show six pentads, pentad 3 - 8, including pentad 7 (31 January - 4 February) in which the heavy rainfall event occurred in Jakarta. In pentad 7, a zonally elongated rain band is formed around 106°E - 119°E, 5°S - 6°S. In that period, Jakarta is located at the western edge of the rain band. There is small amount of rainfall to the north and south of the rain band. The rain band in pentad 7 is consistent with the increase of convergence of horizontal winds at 850 hPa (not shown).

A cold surge is captured through pentad 5 - 7. In pentad 5, a typical Borneo vortex appears; the northeasterly winds over the South China Sea change their direction to southeastward over and around Sumatra Island, and the wind is roughly eastward over West Java. In pentad 6, eastern part of the vortex disappears, and further deformation of the vortex continues. In pentad 7, the winds over the South China Sea become almost northerly. The wind speed increases near West Java and the northerly component increases from pentad 6 to pentad 7. The northerly component of surface wind intensifies upward motion on the northern slope of the mountain range in West Java. The surge event terminates in pentad 8.

In association with the modulation of horizontal wind field, the horizontal distribution of heavy precipitation changes from pentad to pentad. In pentad 5, weak precipitation less than 1 mm hr<sup>-1</sup> covers middle and northern parts of the computational domain with some intensification over the South China Sea. In pentad 6, heavy precipitation areas appear over the South China Sea and the Java Sea. In pentad 7, the former area disappears while the latter moves southward to form the zonally elongated rain band. The rain band disappears in pentad 8.

#### **C-7-4. Discussion**

The Borneo vortex is centered at (1°S, 111°E) in pentad 5, in which precipitation over West Java is relatively weak. Another Borneo vortex event is also captured by the model in pentad 3 (11 - 15 January, Fig. C-7-5a), when the heavy precipitation occurred in the southern tip of Malay Peninsula which faces the South China Sea, as reported by Tangang et al. (2008). Strong convergence associated with a northeasterly cold surge exists over a tip of Malay Peninsula during the event. Although Tangang et al. (2008) argued that this was not a vortex event, based on reanalysis data with the 2.5° × 2.5° resolution, our model output with the 20-km resolution shows the existence of the vortex.

In pentad 7, on the other hand, the vortex disappears, during which the heavy rainfall occurred at Jakarta. This is consistent with the fact that the regions to the south of the South China Sea (namely, the Java Sea) experience enhanced convection when the Borneo vortex is absent (Chang et al. 2005).

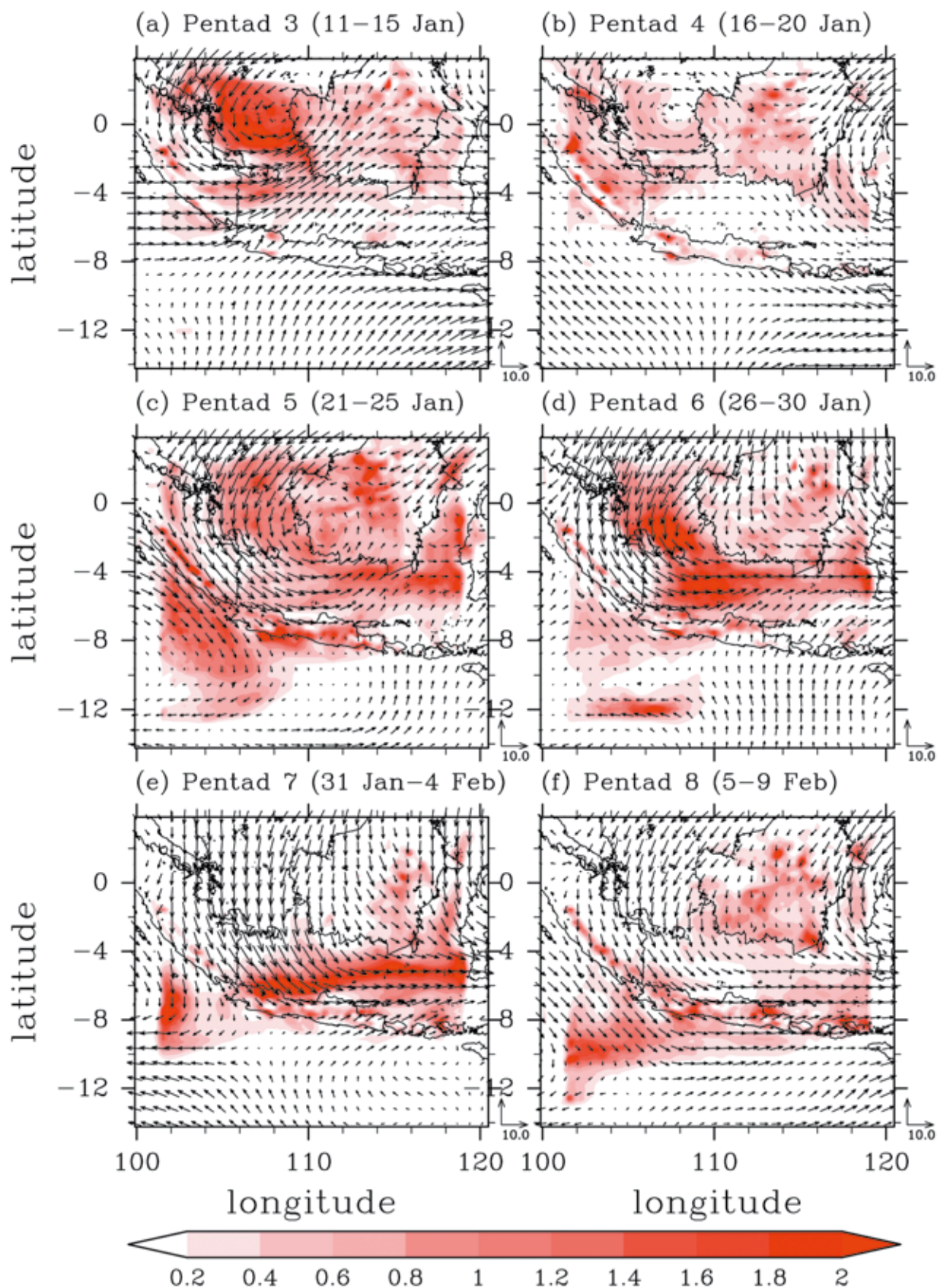


**Fig. C-7-5.** Horizontal distribution of the ensemble mean of the model simulated precipitation rate (mm hr<sup>-1</sup>) and horizontal winds (m s<sup>-1</sup>) at 850 hPa averaged for each pentad. Unit vectors are shown on the right bottom corner in each plot. ‘After Trilaksono et al. (2011).’

### **C-7-5. Conclusions**

A time-lagged ensemble forecast using a regional numerical model is employed to investigate the modulation of precipitation over West Java in the two-month period of January-February 2007. Comparison between the numerical results and the TRMM 3B42 data shows fundamental agreement on the temporal modulation of the spatial distributions of precipitation as shown in Figs. C-7-2 and C-7-3 including the enhancement of precipitation on the time scale of pentad during the period of heavy rainfall, from 31 January to 4 February, in the Jakarta Flood event.

In addition to the modulation of meridional winds reported by Wu et al. (2007), modulation of temperature and relative humidity is also shown in this study. During the two-month period, several monsoon surges are observed, among which only the surge event during the Jakarta Flood event is associated with the cold anomaly. The event is preceded by the Borneo vortex event shown in Fig. C-7-5c. We have shown pentad-to-pentad modulation of synoptic fields of precipitation and only pentad 7, which includes the Jakarta Flood event, has the banded structure of heavy precipitation to the north of Java Island (Fig. C-7-5e).

## **C-8. Simulation of low level cloud over the Western Ghats using a non hydrostatic model<sup>1</sup>**

### **C-8-1. Introduction**

The Western Ghats mountain range along the western coast of India, with an average elevation of about 1200 m, is important for providing sites for hydroelectric power generation. Western India has faced water shortages for many years from lack of rainfall. Artificial rainfall from cloud seeding is one possible solution. To explore this option to enhance rainfall over western India, a series of numerical experiments have been carried out using the high-resolution JMA nonhydrostatic model NHM (Saito et al., 2006). This study simulated the total cloud cover and cloud height at different times of day.

### **C-8-2. The model and simulation of cloud**

NHM was installed on the C-MMACS multiscale forecasting platform. The model explicitly calculates the microphysical processes of hydrometeors such as cloud water, rain, and cloud ice. The typical high-resolution NHM configuration for cloud simulation includes a Lambert conformal mapping, time splitting gravity waves, and split-explicit sound waves. A bulk parameterization scheme that forecasts both the mixing ratio and number concentration is applied to the hydrometeors. The calculation domain of the 5 km NHM was  $2500 \times 2000$  km covering India. The top height of the model domain was about 22 km and employed 40 variable vertical layers. The time integration for up to 48 h was conducted with a time step of 30 s. The NCEP-GFS forecast and analysis were used for initial and boundary conditions.

Figure C-8-1 represents the daily mean cloud coverage simulated 48 h in advance with a resolution of 20 km. The high-resolution (5 km) cloud coverage simulations over the Western Ghats are presented in Figure C-8-2. The three panels represent the simulations at 0500, 1200, and 1700 IST on 14 July 2009.

---

<sup>1</sup> K.C. Gouda and P. Goswami (CSIR C-MMACS)

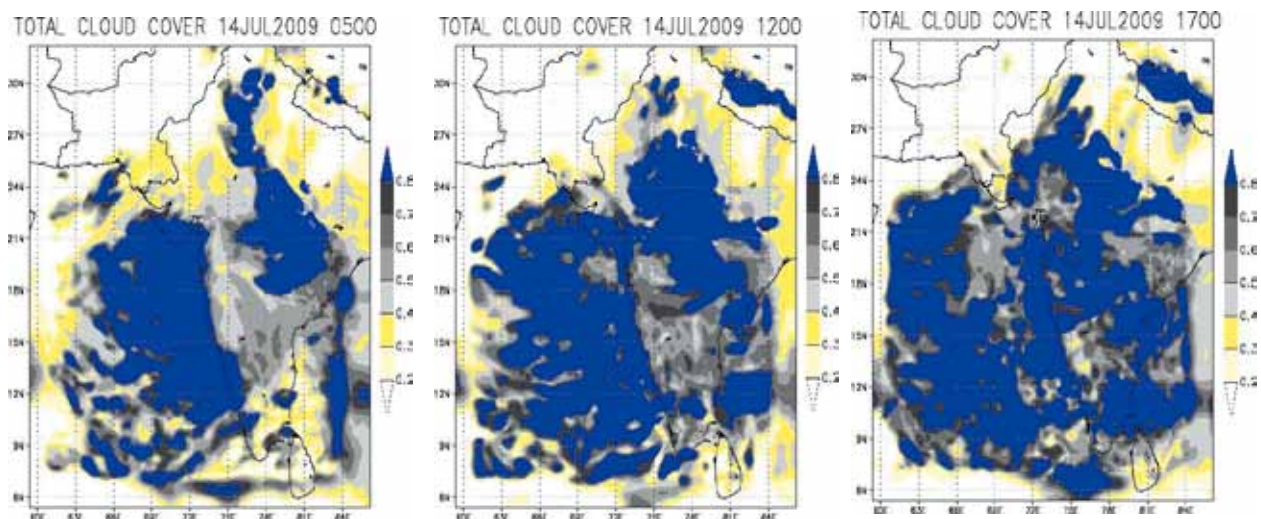


**Fig. C-8-1.** Cloud coverage simulated 48 h in advance at 0500, 1200, and 1700 IST on 14 July 2009 with a resolution of 20 km.

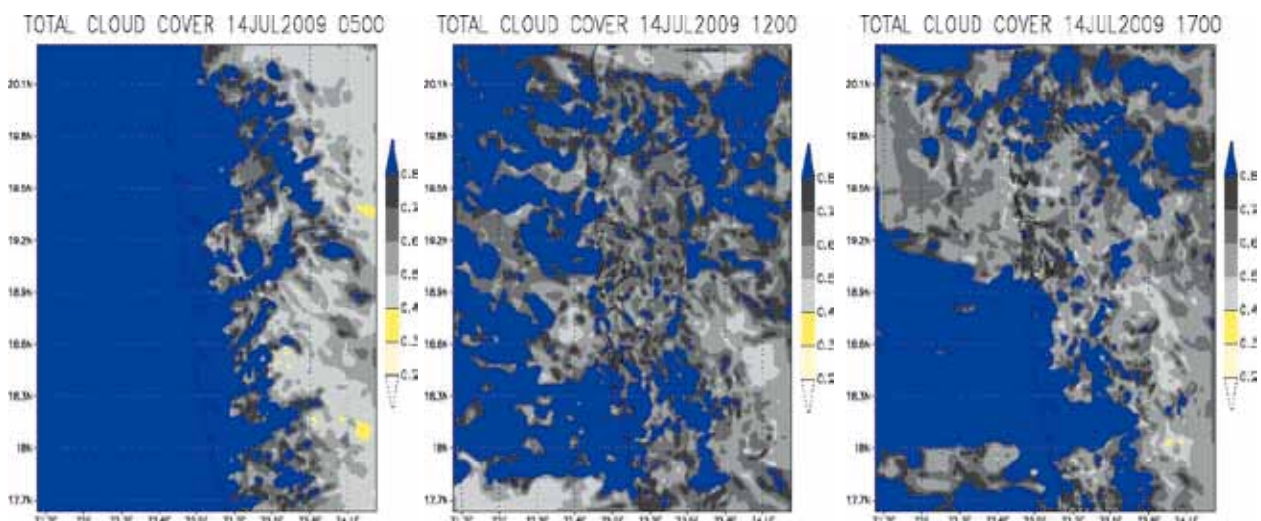


**Fig. C-8-2.** Cloud coverage simulated 48 h in advance at 0500, 1200, and 1700 IST on 14 July 2009 with a resolution of 5 km over the Western Ghats.

### C-8-3. Validation of simulated cloud

A comparison of cloud cover over India from the NHM simulation and MODIS observations for three different days is presented in Figure C-8-3. The simulations are at 20 km resolution, while the observations are at 150 km resolution. The spatial structure of cloud coverage is well captured by the model over the Western Ghats.

The present study needs to be supplemented by extensive diagnostics to understand the effects of high resolution on the simulation of orographic clouds over the Western Ghats. The introduction of high resolution significantly changes model dynamics, and analysis of the circulation features is likely to yield significant insights. The significantly higher skill of the NHM configuration sets the stage for a more detailed diagnostics in terms of cloud coverage. An exciting possibility is to conduct more simulations with different temporal and spatial resolutions and for different seasons to test the robustness of the model in simulating cloud properties.

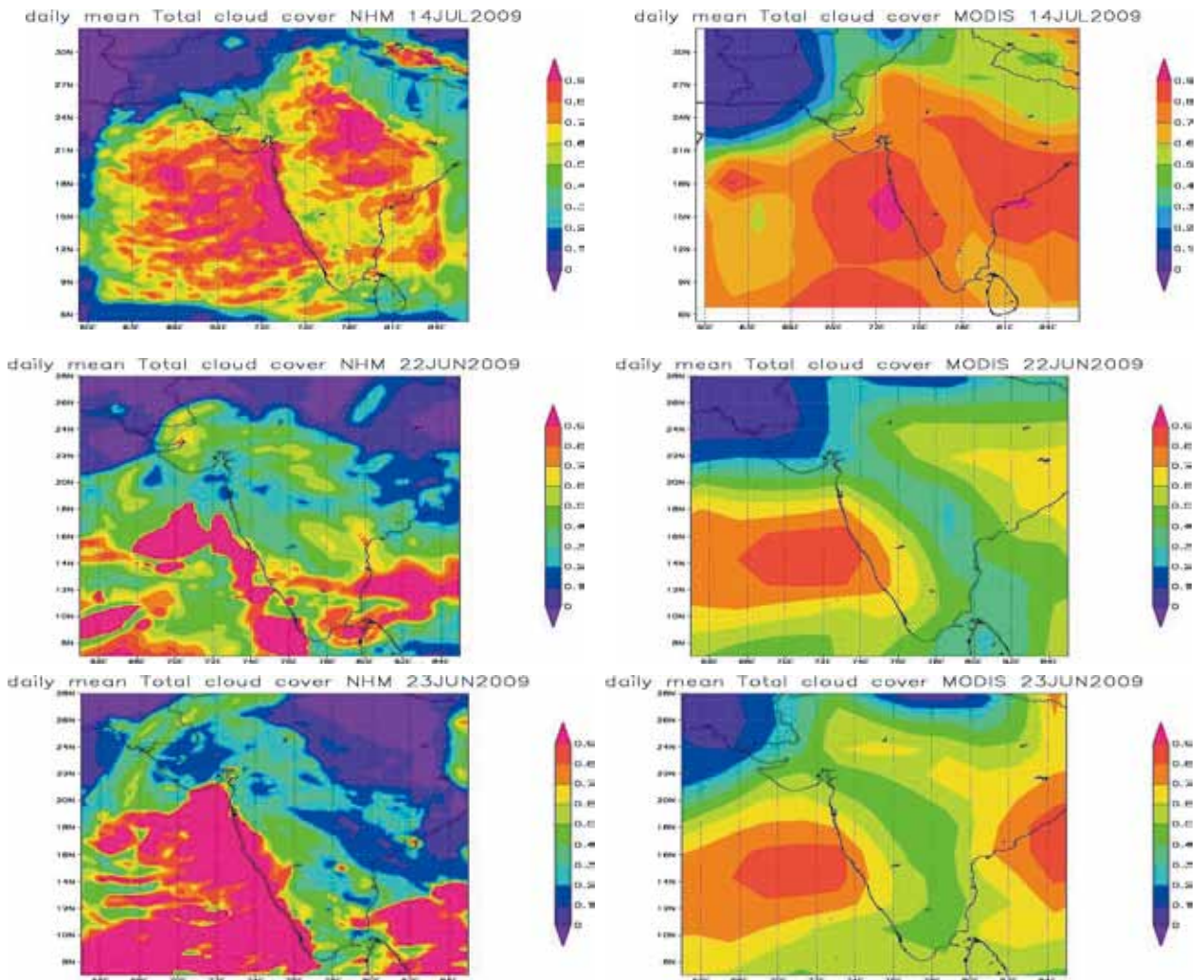


Fig. C-8-3. Comparison of simulated (left) and observed (right; MODIS) daily mean total cloud cover over India on selected days.

**C-8-4. Conclusion**

Success in cloud seeding critically depends on the ability to determine the window of opportunity as well as the right direction of seeding. It is also necessary to generate quantitative knowledge about the response of local cloud systems to different seeding conditions in a cost-effective manner. Simulation and forecasting thus may transform cloud seeding to a precision exercise from what would be otherwise simply blind shooting. With our emphasis on orographic clouds, we have first focused on simulating clouds over the Western Ghats. We found that the present configuration of NHM yields a good cloud simulation over the Western Ghats. Various sensitivity studies of the effect of cloud seeding experiments need to be conducted in NHM.